

# Compton Form Factor Extraction using Quantum Deep Neural Networks

Brandon B. Le<sup>1,\*</sup> and D. Keller<sup>1,†</sup>

<sup>1</sup>*Department of Physics, University of Virginia, Charlottesville, VA 22904, USA.*

(Dated: April 23, 2025)

Extraction tests of Compton Form Factors are performed using pseudodata based on experimental data from Deeply Virtual Compton Scattering experiments conducted at Jefferson Lab. The standard Belitsky, Kirchner, and Muller formalism at twist-two is employed, along with a fitting procedure designed to reduce model dependency similar to traditional local fits. The extraction of the Compton Form Factors is performed using both Classical Deep Neural Networks (CDNNs) and Quantum Deep Neural Networks (QDNNs). Comparative studies reveal that QDNNs outperform CDNNs for this application, demonstrating improved predictive accuracy and precision even for limited model complexity. The results demonstrate the potential of QDNNs for future studies in which quantum algorithms can be fully optimized.

## I. INTRODUCTION

Unraveling the internal structure of the nucleon has been a longstanding goal in hadronic physics, with deeply virtual exclusive processes providing a crucial window into its partonic composition. Among these, Deeply Virtual Compton Scattering (DVCS) stands out as a uniquely sensitive probe of Generalized Parton Distributions (GPDs), which encode the spatial and momentum distributions of quarks and gluons. By linking longitudinal momentum fractions to transverse spatial coordinates, GPDs provide critical insights into the orbital angular momentum carried by partons, bridging the gap between experimental observables and the deeper theoretical understanding of nucleon structure.

Despite their fundamental importance, GPDs cannot be directly extracted from experimental measurements due to their integral appearance in DVCS amplitudes. Instead, Compton Form Factors (CFFs) emerge as a more experimentally accessible alternative, encapsulating the convolution of GPDs with perturbative coefficient functions. These complex-valued functions serve as indirect yet powerful observables, enabling the study of quark and gluon distributions through measurable quantities such as cross-sections and asymmetries. However, the extraction of CFFs remains a formidable challenge, as they are embedded in helicity amplitudes and entangled with quantum interference effects. This may necessitate the advancement of analysis techniques to go beyond classical methods, leveraging approaches capable of capturing the quantum correlations inherent in the DVCS process. In this context, quantum deep neural networks (QDNNs) offer a promising approach to the systematic extraction of quantum information pertaining to partonic degrees of freedom, enhancing our ability to measure and interpret the quantum structure of the nucleon.

QDNNs are neural network architectures that take advantage of quantum mechanics to process information.

Unlike classical deep learning models that rely on traditional computation, QDNNs employ quantum circuits as trainable components, allowing them to explore complex, high-dimensional function spaces more efficiently. Libraries such as PennyLane and Quantum TensorFlow provide frameworks to construct and train QDNNs using hybrid quantum-classical approaches. These frameworks enable the encoding of classical data into quantum states, manipulation through quantum circuits, and extraction of results via measurement processes. PennyLane is designed to integrate quantum computing with machine learning and automatic differentiation techniques, allowing users to build quantum nodes (or “QNodes”) that can be optimized in conjunction with classical deep learning architectures. Quantum TensorFlow extends Google’s TensorFlow to incorporate quantum computation, enabling quantum variational circuits to be trained using classical gradient descent methods. These tools provide a seamless way to incorporate quantum algorithms into machine learning tasks, facilitating the study of quantum-enhanced feature extraction, pattern recognition, and regression tasks, particularly those of a quantum nature.

One of the compelling applications of QDNNs is in the extraction of kinematically sensitive parameters from helicity amplitudes, such as the CFFs in deeply virtual processes. In DVCS, the helicity amplitudes of the interaction encode critical information about the partonic structure of the nucleon. These amplitudes are complex-valued functions of kinematic variables like the momentum transfer squared, the Bjorken scaling variable, and the photon virtuality. Extracting these CFFs from experimental measurements is challenging because of limitations in constraints, both measured and mathematical, but also because of the inherent interference with the Bethe-Heitler process. The interference term in DVCS and Bethe-Heitler processes emerges because the final state (electron, nucleon, and photon) is produced by two coherent quantum amplitudes that interfere constructively or destructively. This is a direct consequence of quantum superposition and phase coherence. Traditionally, machine learning methods, particularly feed-forward

---

\* sxh3qf@virginia.edu

† dustin@virginia.edu

deep neural networks, have been employed to fit experimental data and extract the underlying parameters. However, classical models may not be optimal when dealing with problems involving interference effects, quantum entanglement, and correlations between partonic degrees of freedom. QDNNs provide an alternative approach that naturally accommodates such quantum mechanical correlations. By encoding kinematic inputs into quantum states and using quantum variational circuits to process them, QDNNs can potentially uncover structures in the data that classical networks fail to capture.

The non-perturbative structure of helicity amplitudes in processes like DVCS often involves complex transformations between Generalized Parton Distributions (GPDs), CFFs, and measurable observables. Since QDNNs operate in a Hilbert space, they inherently support the representation of complex-valued functions, making them well-suited for approximating helicity amplitudes. Specifically, quantum feature maps in PennyLane allow one to encode cross-section data into quantum states, which can then be evolved using parameterized quantum circuits to optimize for the best representation of the underlying CFFs. A variational quantum circuit (VQC) can be trained to approximate the mapping between experimental observables, such as beam-spin asymmetries, and the CFFs that define them. This process involves quantum data encoding, where experimental data, including kinematic variables, are transformed into quantum states using amplitude or basis encoding, effectively translating kinematic dependencies into quantum states. The next step is quantum circuit evolution, in which a series of quantum gates parameterized by tunable angles is applied to transform the encoded information. These gates are chosen to represent the functional relationship between helicity amplitudes and observables. Finally, measurement and training are performed by extracting relevant quantities and using hybrid quantum-classical optimization methods, such as quantum natural gradient descent, to adjust the parameters in the quantum circuit to fit the data.

By leveraging quantum entanglement and interference, QDNNs can capture nontrivial correlations between observables that are difficult for classical models to learn efficiently. In CFF extraction, classical neural networks have to approximate real and imaginary parts separately, often missing interference effects that are intrinsic to the DVCS amplitude. A QDNN, however, can process this information holistically by leveraging superposition and quantum state evolution, which naturally preserve these quantum correlations. Additionally, quantum-enhanced feature spaces allow for a more expressive representation of the functional dependencies of helicity amplitudes. This is particularly useful in scenarios where experimental uncertainties and systematic errors obscure direct parameter extraction. Since QDNNs operate in a higher-dimensional Hilbert space, they can encode more complex functional mappings, potentially leading to more accurate determinations of observables like beam-spin and

target-spin asymmetries, which are crucial in probing the nucleon structure.

With the rapid advancement of near-term quantum processors, such as those developed by IBM, Google, and Rigetti, experimental physics stands at the threshold of utilizing QDNNs for real-world data analysis. A promising approach involves integrating quantum machine learning with Monte Carlo sampling methods to systematically propagate experimental errors through the quantum model, improving the robustness of extracted parameters like CFFs. The application of Quantum DNNs in libraries like PennyLane and Quantum TensorFlow offers a new paradigm for extracting quantum-mechanical observables in high-energy physics. By exploiting quantum feature spaces, entanglement, and parameterized quantum circuits, these models can potentially outperform classical approaches in unraveling the helicity structure of deeply virtual processes like DVCS. As quantum hardware continues to improve, QDNNs may soon become indispensable tools for analyzing quantum field-theoretic processes, leading to deeper insights into the fundamental structure of matter. This approach may enhance the extraction fidelity of critical observables and open new avenues for studying the quantum correlations embedded within the hadronic structure.

High-statistics, finely binned data from experimental facilities such as Jefferson Lab have provided insight into the valence quark region, while complementary measurements from HERA and COMPASS have explored the role of sea quarks and gluons in deeply virtual processes. These data sets serve as the basis for generating pseudo-data and set initial benchmarks for developing and validating machine learning techniques, enabling systematic comparisons between CDNNs and QDNNs.

Looking ahead, future experimental programs such as the Electron-Ion Collider (EIC) will dramatically expand the kinematic reach of DVCS measurements, particularly in the sea quark- and gluon-dominated regime. The combination of these new data with advanced QDNN-based extraction techniques offers a powerful opportunity to deepen our understanding of the nucleon's internal structure. By leveraging quantum machine learning to disentangle the intricate relationships between spatial and momentum distributions, these methods could bring us closer to achieving a fully resolved three-dimensional mapping of partonic structure, uncovering new aspects of hadronic physics that remain inaccessible to classical approaches.

In this work, we demonstrate some very basic applications of QDNNs for information extraction and develop some metrics for comparison. Then we perform some extraction testing using a standard local fit involves fitting a single observables at fixed kinematics, across the independent variable  $\phi$ , the azimuthal angle between the lepton and hadron scattering planes. Local fitting relies on the chosen framework of general approximation, such as twist truncation, leading-order contributions, and the dominance of some CFFs. At the highest approxi-

mation, the parametrization of observables, such as the cross-section, in terms of CFFs is not unique as it is convention-dependent since it violates the required symmetries which are restored by contributions that are formally suppressed by powers of  $1/Q$ , dubbed higher-twist corrections. In this regard, the extracted CFF depends on the choice of the observable formalism [1–6].

While local fits offer the advantage of being potentially model-independent, extracting unique CFFs for fixed kinematics remains a formidable challenge, particularly when the number of available observables is limited, reducing the constraints in the fit. Since CFFs can vary freely within a high-dimensional parameter space, standard  $\chi^2$  minimization methods often suffer from inconsistent local minima, leading to significant uncertainties in their extraction, even in the most rigorous analyses. As experimental datasets continue to grow in both quantity and precision, particularly with the inclusion of multiple polarized observables, the issue of data sparsity is gradually being mitigated. However, to fully capitalize on these advancements, it is equally crucial to refine and enhance the extraction techniques, ensuring they are capable of handling the increasing complexity and richness of the data.

We employ a straightforward approach using simple feedforward architectures and, similar to previous work [7, 8], incorporate the helicity amplitude formalism directly into the loss function during the backpropagation of error. To account for experimental uncertainties, we propagate errors through a Monte Carlo ensemble of replicas [9], where the cross-section data is resampled within its experimental uncertainty. This ensemble generates a distribution of extracted CFFs, with the width of the distribution reflecting both the inherent experimental errors and the uncertainties arising from the fitting procedure.

We focus on the least constrained observable case: the unpolarized DVCS cross-section. We adopt the formalism developed by Belitsky and Müller, specifically the BKM10 framework [3], which defines the structure of the helicity amplitudes used in the extraction. While this approach is tailored to the BKM10 formalism, the extraction method itself is general and can be adapted to alternative theoretical frameworks as needed. Future work will explore an expanded approach aimed at minimizing potential biases introduced by the choice of helicity amplitude formalism. A brief overview of the BKM10 formalism will be provided in the next section.

In this study, we compare the performance of CDNNs and QDNNs in the extraction of CFFs, using a consistent theoretical framework and a new quantum metric. To ensure a direct comparison, we adopt the BKM10 formalism [3] for both approaches, maintaining uniformity in the helicity amplitude structure used in the loss function. We also focus on quantifying and matching model complexity. By applying identical pseudo input data and theoretical constraints, we systematically evaluate how QDNNs enhance the extraction process relative to

CDNNs, particularly in capturing quantum correlations and mitigating fit ambiguities. The BKM10 formalism, which will be briefly discussed in the next section, provides a well-established foundation for this comparative study, allowing us to isolate the advantages introduced by quantum machine learning techniques.

The remainder of this paper is organized in the following way. In Section II, we provide a detailed description of the theoretical framework for the DVCS channel and describe how CFFs are relevant to the extraction process. In Section VII we present the experimental data to be used to generate the pseudodata. In Section IX, we describe how the pseudodata is produced and perform a standard DNN local fit for comparison. We then perform some basic CDNN and QDNN comparison with regression and classification task. And the perform the extraction of the DVCS CFFs with both CDNN and QDNN. In Section X, we present our conclusions and discuss future outlooks for this research.

## II. THEORY FRAMEWORK

The DVCS process studies the virtual Compton scattering in deep-inelastic kinematics at the leading order in perturbative QCD. DVCS is dominated by single-quark scattering, and therefore the amplitude can be expressed in terms of the off-forward parton distributions. In the helicity-independent case, a virtual photon scatters from an unpolarized electron beam of energy  $k$  off an unpolarized proton leading to the 4-fold photon electroproduction differential cross-section:

$$\frac{d^4\sigma}{dx_B dQ^2 dt|d\phi} = \frac{\alpha^3 x_B y^2}{8\pi Q^4 \sqrt{1+\epsilon^2}} \frac{1}{e^6} |\mathcal{T}|^2. \quad (1)$$

The phase space of this process is parameterized by the Bjorken variable,  $x_B = Q^2/2pq$ , the four-momentum  $q = k - k'$  carried by the virtual photon of mass  $Q^2 = -q^2 = -(k - k')^2$ , the squared momentum transfer between the initial and final protons  $t = \Delta^2$  with  $\Delta = p' - p$  and the lepton energy loss  $y = (p \cdot q)/(p \cdot k)$ . The azimuthal angle  $\phi$  between the leptonic and hadronic planes is defined in the Trento convention [10]. In the cross-section,  $\alpha = e^2/(4\pi)$  is the fine structure constant, and  $\epsilon = 2x_B M/Q^2$  where  $M$  is the proton mass.

The photon electroproduction cross-section is sensitive to the coherent interference of the DVCS amplitude with the Bethe-Heitler (BH) amplitude. The DVCS process, namely, the electroproduction of a photon off a proton with the exchange of a photon with virtuality,  $Q^2$ , much larger than the momentum transfer squared  $t$ , hypothetically provides one of the cleanest probes of the GPDs. The BH is an easily calculated electromagnetic process, where a real photon is emitted by the initial or the final lepton. Therefore both, DVCS and BH channels contain the same final states, which can not be distinguished experimentally, and the total photon electroproduction

amplitude squared is given by the linear superposition of these two processes:

$$|\mathcal{T}|^2 = |\mathcal{T}_{DVCS}|^2 + |\mathcal{T}_{BH}|^2 + \mathcal{I}, \quad (2)$$

with the interference term  $\mathcal{I}$  being:

$$\mathcal{I} = \mathcal{T}_{DVCS}\mathcal{T}_{BH}^* + \mathcal{T}_{DVCS}^*\mathcal{T}_{BH}. \quad (3)$$

The BH contribution is computed exactly in [1]. It is well known from QED calculations with great precision in terms of the proton electromagnetic form factors in the range of  $-t < 0.4 \text{ GeV}^2$  and will not be discussed in detail. The unpolarized BH amplitude is given by:

$$|\mathcal{T}_{BH}|^2 = \frac{e^6}{x_B^2 y^2 (1 + \epsilon^2)^2 t \mathcal{P}_1(\phi) \mathcal{P}_2(\phi)} \sum_{n=0}^2 c_n^{BH} \cos(n\phi). \quad (4)$$

The harmonic terms  $c_n^{BH}$  of the BH amplitude squared depend only upon bilinear combinations of the electromagnetic form factors  $F_1(t)$  and  $F_2(t)$ , which are computed from Kelly's parametrization [11]. The factors  $\mathcal{P}_1(\phi)$  and  $\mathcal{P}_2(\phi)$  are the electron propagators in the BH amplitude.

The DVCS amplitude encodes the partonic structure of the nucleon given by the Compton tensor  $T^{\mu\nu}$  [12] where the observables for the extraction of GPDs emerge. The proven QCD factorization theorem on DVCS [13, 14], permits to express the Compton tensor into perturbative coefficients and the long-distance dynamics that give rise to the GPDs and introduce the handbag diagrams twist expansion. The proven QCD factorization theorem on DVCS [13, 14], which is valid only at values of  $t$  such that  $-t \ll Q^2$ , permits separating the Compton tensor into the hard scattering process at short distances between the virtual photon, electron, and quarks, which can be calculated using perturbative QCD, from the soft, long-distance dynamics that give rise to the non-perturbative GPDs that describe the internal structure of hadrons. The soft interactions of the struck parton by the virtual photon with the rest of the proton can be viewed as the exchange of partons of virtuality of the order of  $Q^2$ . Powers of  $1/Q$  suppress their contribution to the cross-section of the process as the number of exchanged partons increases. The hard part of scattering processes is described using a perturbative expansion in increasing orders of the strong coupling constant  $\alpha_s$ . This perturbative expression of the hard part in the scattering process is known as the coefficient function.

At leading order (LO) in perturbative QCD and leading twist (LT) approximation, four independent proton GPDs can be accessed in the DVCS process:  $H$ ,  $E$ ,  $\tilde{H}$  and  $\tilde{E}$ . These four GPDs depend on three variables:  $x$ ,  $\xi$  and  $t$  where the latter two are experimental parameters with the skewness  $\xi = x_B/(2 - x_B)$  at leading twist and  $x \pm \xi$  the light-cone longitudinal momentum fraction of the struck quark before (“+” sign) and after (“-” sign) the scattering, such that the difference in the momentum fraction of the quark before absorbing the virtual

photon and after the emission of the real photon is given by  $2\xi$ , resulting in a squared four-momentum transfer  $t$  to the nucleon. This gives rise to the division of the GPDs into two distinct regions, each carrying entirely different physical interpretations. In the region where the momentum fraction  $x$  exceeds  $\xi$  or falls below  $-\xi$  the GPDs are interpreted as the amplitudes governing the emission and reabsorption of a parton. Conversely, within region encompassing  $-\xi < x < \xi$ , GPDs resemble distribution amplitudes governing the emission or absorption of a parton-antiparton pair.

A significant challenge encountered in the study of GPDs stems from their appearance in the amplitude of DVCS as integrals over the momentum fraction variable  $x$  ranging from -1 to 1, a consequence of implied quark loop. Since  $x$  cannot be measured experimentally, the DVCS cross-section is instead parametrized in terms of CFFs that are directly accessible. The twist-2 CFFs are weighted integrals of these twist-2 GPDs over  $x$  or combinations of GPDs at the line  $x = \xi$ . The four quark CFFs  $\mathcal{F} = \{\mathcal{H}, \mathcal{E}, \tilde{\mathcal{H}}, \tilde{\mathcal{E}}\}$  are related to the quark GPDs  $F = \{H, E, \tilde{H}, \tilde{E}\}$  as:

$$\mathcal{F}(\xi, t) \equiv \sum_q \int_{-1}^1 dx C_q^{[\mp]}(x, \xi) F_q(x, \xi, t), \quad (5)$$

where the leading order complex-valued coefficient function related to the hard scattering part [1, 15] is:

$$C_q^{[\mp]} = e_q^2 \left( \frac{1}{\xi - x - i0} \mp \frac{1}{\xi + x - i0} \right), \quad (6)$$

$e_q$  is the charge of quarks in units of proton charge and the summation runs over all quark flavors  $q$ . Using the residue theorem, it is possible to decompose the integral (5) so that each CFF contains two real quantities:

$$\mathcal{F}(\xi, t) = \Re\mathcal{F}(\xi, t) + i\Im\mathcal{F}(\xi, t), \quad (7)$$

where

$$\Re\mathcal{F}(\xi, t) = \sum_q \mathcal{P} \int_0^1 dx \left( \frac{1}{\xi - x} \mp \frac{1}{\xi + x} \right) F_q^{[\mp]}(x, \xi, t), \quad (8)$$

$$\Im\mathcal{F}(\xi, t) = \pi \sum_q F_q^{[\mp]}(\xi, \xi, t). \quad (9)$$

Here,  $\mathcal{P}$  denotes the Cauchy principal value and,

$$F_q^{[\mp]}(x, \xi, t) = e_q^2 [F_q(x, \xi, t) \mp F_q(-x, \xi, t)]. \quad (10)$$

The top sign in equations (5)-(10), corresponds to the unpolarized GPDs ( $H, E$ ) and the bottom sign applies to the polarized GPDs ( $\tilde{H}, \tilde{E}$ ). Equations (8) and (9) show that observables sensitive to the imaginary part of the CFFs will only contain information along the line  $x = \pm\xi$ , whereas the real part probes GPD integrals over the momentum fraction  $x$ . Given the complicated

kinematic dependence of the GPDs, retrieving them from CFFs is therefore a major challenge of the field, known as the deconvolution problem [16]. Thus, the maximum model-independent information which can be extracted from the DVCS reaction at leading twist are 8 CFFs, which depend on two variables,  $\xi$  and  $t$ , at QCD leading order. There is an additional  $Q^2$  dependence in the CFFs (and in the GPDs) if QCD evolution is taken into account.

The unpolarized beam and unpolarized target cross-sections rely on the Belitsky-Kirchner-Muller DVCS formulation (BKM10) [3] and we focus on the case where only twist-2 CFFs enter the cross-section. In this case, the squared DVCS amplitude is a bilinear combination of the CFFs contained in the coefficient  $C^{DVCS}(\mathcal{F}, \mathcal{F}^*)$ :

$$|\mathcal{T}^{DVCS}|^2 = \frac{e^6}{y^2 Q^2} \left\{ 2 \frac{2 - 2y + y^2 + \frac{\epsilon^2}{2} y^2}{1 + \epsilon^2} C^{DVCS}(\mathcal{F}, \mathcal{F}^*) \right\}. \quad (11)$$

The DVCS amplitude is contingent on the four complex-valued twist-2 CFFs consisting of two real magnitudes, leading to the emergence of eight distinct CFF parameters. This intricate multiplicity of parameters underscores the complexity involved in their extraction process. A noteworthy aspect in this context is that, under this approximation, the DVCS process lacks dependence on the azimuthal angle. This can be an advantage in the extraction procedure by taking it as a free parameter.

The unpolarized interference term in Eq. (2), is a linear combination of CFFs, with the following harmonic structure:

$$\mathcal{I} = \frac{e^6}{x_B y^3 t \mathcal{P}_1(\phi) \mathcal{P}_2(\phi)} \sum_{n=0}^3 c_n^{\mathcal{I}} \cos(n\phi), \quad (12)$$

where the Fourier coefficients are:

$$c_n^{\mathcal{I}} = C_{++}^n \Re C_{++}^{\mathcal{I},n}(\mathcal{F}) + C_{0+}^n \Re C_{0+}^{\mathcal{I},n}(\mathcal{F}_{eff}) + C_{-+}^n \Re C_{-+}^{\mathcal{I},n}(\mathcal{F}_{\mathcal{T}}). \quad (13)$$

The double helicity-flip gluonic CFFs amplitudes,  $C_{-+}^{\mathcal{I},n}(\mathcal{F}_{\mathcal{T}})$ , are formally suppressed by  $\alpha_s$  and will be neglected here.  $C_{++}^{\mathcal{I},n}(\mathcal{F})$  and  $C_{0+}^{\mathcal{I},n}(\mathcal{F}_{eff})$  are the helicity-conserving and the helicity-changing amplitudes respectively. The helicity-changing amplitudes also contain the contribution from twist-3 CFFs implicit in the effective CFFs ( $\mathcal{F}_{eff}$ ). Thus, we chose a framework where only the helicity-conserving amplitudes are considered which contain only pure twist-2 CFFs contributions, similarly to [17]. In that way, we set more constraints on the physics with the same amount of data, giving up to some information at the expense of greater accuracy in the remaining parameters. The helicity-conserving amplitudes are

given by:

$$\Re C_{++}^{\mathcal{I},n}(\mathcal{F}) = \Re C^{\mathcal{I}}(\mathcal{F}) + \frac{C_{++}^{V,n}}{C_{++}^n} \Re C^{\mathcal{I},V}(\mathcal{F}) + \frac{C_{++}^{A,n}}{C_{++}^n} \Re C^{\mathcal{I},A}(\mathcal{F}). \quad (14)$$

The complete expressions of the kinematic coefficients  $C_{++}^n$ ,  $C_{++}^{V,n}$  and  $C_{++}^{A,n}$  are given in [3]. The  $C^{\mathcal{I}}$ ,  $C^{\mathcal{I},V}$  and  $C^{\mathcal{I},A}$  terms are a linear combination of the CFFs:

$$C^{\mathcal{I}}(\mathcal{F}) = F_1 \mathcal{H} + \xi(F_1 + F_2) \tilde{\mathcal{H}} - \frac{t}{4M^2} F_2 \mathcal{E} \quad (15)$$

$$C^{\mathcal{I},V}(\mathcal{F}) = \frac{x_B}{2 - x_B + x_B \frac{t}{Q^2}} (F_1 + F_2) (\mathcal{H} + \mathcal{E}) \quad (16)$$

$$C^{\mathcal{I},A}(\mathcal{F}) = \frac{x_B}{2 - x_B + x_B \frac{t}{Q^2}} (F_1 + F_2) \tilde{\mathcal{H}} \quad (17)$$

In this specific scenario, the interference cross-section becomes reliant solely on three real-valued CFFs:  $\Re \mathcal{H}$ ,  $\Re \mathcal{E}$  and  $\Re \tilde{\mathcal{H}}$ . The real parts of the CFFs  $\Re \mathcal{H}$ ,  $\Re \mathcal{E}$  and  $\Re \tilde{\mathcal{H}}$  arise from the dispersive integrals of the corresponding GPDs  $H$ ,  $E$ , and  $\tilde{H}$ , representing their convolution with the hard scattering kernel.  $\Re \mathcal{H}$  dominates the DVCS amplitude for unpolarized targets and reflects the spatial-momentum distribution of unpolarized quarks.  $\Re \mathcal{E}$  is sensitive to nucleon helicity-flip and provides access to parton orbital angular momentum via Ji's sum rule.  $\Re \tilde{\mathcal{H}}$  encodes the distribution of polarized quarks and governs the longitudinal spin structure, playing a leading role for polarized targets. Additionally, accounting for the constant nature of the pure DVCS cross-section in terms of the azimuthal angle, the total number of parameters that need to be extracted is reduced to four. We chose this framework to make the comparison of CDNN and QDNN extractions more direct. The reduction in the parameter count simplifies the extraction process relative to the full eight-parameter scenario, while still preserving the most relevant aspects of the phenomenological information. This simplified parameter space facilitates a more manageable data analysis and modeling, making a more straightforward demonstration of the extraction steps of the essential parameters from experimental data. A separate future paper will investigate directly the quantum advantage in extracting the complex valued CFFs.

### III. QUANTUM DEEP NEURAL NETWORKS

QDNNs integrate principles of quantum mechanics into deep learning architectures, offering a novel computational framework distinct from classical deep neural networks (CDNNs). While CDNNs process data using weighted sums and nonlinear activation functions in

Euclidean space, QDNNs manipulate quantum states in Hilbert space via unitary transformations. PennyLane, a quantum computing library, enables the development of these models by integrating quantum circuits—either simulated or executed on quantum hardware—into classical machine learning frameworks. Although the long-term goal is to deploy QDNNs on fault-tolerant quantum processors, current implementations primarily rely on simulators, which serve as an efficient platform for testing and optimizing quantum neural architectures. These approaches offer alternative algorithmic methods that, in some cases, complement classical deep learning.

In a classical neural network, each layer applies a transformation of the form  $h = \sigma(Wx + b)$ , where  $W$  is a weight matrix,  $b$  is a bias term, and  $\sigma$  is a nonlinear activation function. In contrast, QDNNs replace these transformations with quantum operations acting on qubits. A system of  $n$  qubits exists in a  $2^n$ -dimensional complex Hilbert space, where its quantum state is represented as a superposition of computational basis states,

$$|\psi\rangle = \sum_{i=0}^{2^n-1} c_i |i\rangle,$$

where  $c_i \in \mathbb{C}$  are complex probability amplitudes satisfying the normalization condition

$$\sum_{i=0}^{2^n-1} |c_i|^2 = 1.$$

This normalization ensures that the total probability of measuring any basis state sums to unity, preserving the probabilistic interpretation inherent in quantum mechanics. The evolution of the quantum state is governed by unitary operators, which preserve the norm of the state vector and satisfy the condition,

$$U^\dagger U = I,$$

where  $U^\dagger$  is the Hermitian conjugate (conjugate transpose) of  $U$ , and  $I$  is the identity matrix. The application of a unitary transformation to a quantum state results in

$$|\psi'\rangle = U|\psi\rangle.$$

The unitary operations in a QDNN are represented as matrices  $U \in \mathbb{C}^{2^n \times 2^n}$ , ensuring that each operation is a valid quantum transformation that preserves inner products and maintains the reversibility required by quantum mechanics. In contrast to classical neural networks, which apply affine transformations followed by nonlinear activation functions, QDNNs process information using sequences of unitary transformations, where each layer consists of a set of parameterized quantum gates.

A simple example of a single-qubit unitary transformation is a rotation about the  $x$ -axis, given by the Pauli rotation matrix

$$R_x(\theta) = e^{-i\theta X/2} = \begin{pmatrix} \cos(\theta/2) & -i \sin(\theta/2) \\ -i \sin(\theta/2) & \cos(\theta/2) \end{pmatrix}.$$

Similarly, rotations about the  $y$ - and  $z$ -axes are defined by

$$R_y(\theta) = e^{-i\theta Y/2}, \quad R_z(\theta) = e^{-i\theta Z/2}.$$

A full quantum circuit is composed of multiple layers of these parameterized unitary transformations, interspersed with entangling gates that introduce correlations between qubits. The final quantum state of a circuit with  $L$  layers is expressed as

$$|\psi_{\text{final}}\rangle = U_L U_{L-1} \cdots U_1 |0\rangle^{\otimes n}.$$

Encoding classical data into quantum circuits is a fundamental step in constructing QDNNs. One commonly used encoding technique is angle embedding, where classical input values are mapped to rotation angles of single-qubit gates. Given an input feature  $x$ , the encoding is performed via the transformation,

$$R_x(x)|0\rangle = e^{-ixX/2}|0\rangle.$$

Once encoded, additional parameterized unitary gates modify the quantum state based on learnable parameters. The role of entanglement in QDNNs is particularly significant, as it enables the representation of highly non-trivial correlations that classical networks may require exponentially many parameters to approximate. Entanglement is introduced using multi-qubit gates such as the controlled-NOT (CNOT) gate, represented as the unitary matrix

$$\text{CNOT} = \begin{pmatrix} 1 & 0 & 0 & 0 \\ 0 & 1 & 0 & 0 \\ 0 & 0 & 0 & 1 \\ 0 & 0 & 1 & 0 \end{pmatrix}.$$

By incorporating these entangling operations, QDNNs exploit quantum mechanical effects that enhance the expressivity and representational power of the model.

The final step in a QDNN is measurement, which extracts classical information from the quantum state. In quantum mechanics, measurements correspond to taking the expectation values of Hermitian observables. The expectation value of an observable  $O$  for a quantum state  $|\psi\rangle$  is computed as

$$\langle O \rangle = \langle \psi | O | \psi \rangle.$$

For Pauli-Z measurements, this simplifies to

$$\langle Z \rangle = \langle \psi | Z | \psi \rangle = |\langle 0 | \psi \rangle|^2 - |\langle 1 | \psi \rangle|^2.$$

These expectation values form the classical outputs of a QDNN, which can be further processed using classical deep learning methods. The full QDNN architecture, therefore, consists of data encoding, a sequence of parameterized unitary transformations, entangling operations, and final measurement.

To train a QDNN, the parameters  $\theta$  in the quantum gates are optimized to minimize a loss function, typically defined as

$$f(\theta) = \langle \psi(\theta) | O | \psi(\theta) \rangle.$$

Unlike CDNN which compute gradients via backpropagation, QDNNs employ the parameter shift rule to estimate derivatives of expectation values. This quantum gradient calculation is given by

$$\frac{d}{d\theta} \langle Z \rangle = \frac{\langle Z(\theta + \pi/2) \rangle - \langle Z(\theta - \pi/2) \rangle}{2}.$$

This ensures that QDNNs can be trained using familiar gradient-based optimization techniques while preserving quantum coherence.

QDNNs offer a compelling advantage over CDNN due to their ability to exploit the exponential dimensionality of quantum state space. A quantum system with  $n$  qubits exists in a Hilbert space of dimension  $2^n$ , allowing QDNNs to represent highly complex transformations with far fewer parameters than classical networks, which scale polynomially. Additionally, quantum entanglement enables QDNNs to model intricate correlations that classical networks struggle to capture efficiently. Superposition further enhances expressivity by allowing quantum states to encode multiple computational pathways simultaneously.

One of the most promising theoretical advantages of QDNNs is their trainability in high-dimensional spaces. CDNNs, particularly in complex optimization landscapes, suffer from barren plateaus, where gradients vanish exponentially as the model scales. Quantum circuits, when properly designed, mitigate this issue through entanglement-assisted learning, preserving trainability across larger architectures. Quantum kernel methods and variational quantum circuits have already demonstrated superior learning efficiency in structured data representations.

Despite these theoretical advantages, practical QDNN implementation faces challenges due to hardware limitations, including noise, decoherence, and limited qubit connectivity. PennyLane facilitates the development of QDNNs by providing a robust framework for hybrid quantum-classical machine learning, enabling direct comparisons between quantum and classical networks. While most PennyLane computations are currently executed on quantum simulators, which explicitly store quantum states as vectors in Hilbert space and evolve them using matrix multiplications, future developments in quantum hardware may enable large-scale deployment of QDNNs on real quantum processors.

As quantum computing technology advances, QDNNs may surpass CDNNs in efficiency and accuracy for specialized tasks. Theoretically, deep quantum circuits with polynomial-depth entangling layers could approximate function classes exponentially faster than classical models. While the realization of quantum advantage in deep

learning remains an open question, QDNNs represent a promising avenue for integrating quantum mechanics into artificial intelligence, unlocking new possibilities in optimization, generative modeling, and high-dimensional learning.

The advantage of QDNNs lies in their ability to leverage quantum superposition and entanglement to explore quantum features or function spaces that classical networks may struggle to approximate efficiently. The quantum algorithms themselves may also offer more efficient computation and representation of the complexity of the system. One key advantage is the exponential growth of the Hilbert space, where a quantum system with  $n$  qubits exists in a space of dimension  $2^n$ , allowing quantum circuits to represent highly complex transformations with far fewer parameters than classical networks, which scale polynomially. Additionally, quantum circuits can efficiently represent certain functions that classical models struggle to approximate without an exponential number of parameters, particularly those involving highly entangled correlations.

Quantum superposition enables a richer feature representation by allowing multiple computational pathways to be explored simultaneously, while entanglement further enhances the expressivity of quantum circuits by capturing intricate correlations that may be difficult for classical models to learn. This can be particularly beneficial for datasets with hidden structures that quantum circuits can exploit more naturally. Moreover, quantum models have shown potential speedups for specific tasks, such as quantum kernel methods and variational quantum circuits, which have demonstrated the ability to learn complex patterns with fewer computational resources compared to classical methods.

Another important aspect is trainability. CDNNs often suffer from vanishing gradients in high-dimensional parameter spaces, a problem known as barren plateaus. Well-designed quantum circuits, however, can mitigate this issue through entanglement-assisted learning dynamics, making them more efficient in certain scenarios. Despite these advantages, the practical realization of quantum models remains an ongoing challenge due to hardware limitations, and the key is identifying problems where quantum circuits provide a significant edge over classical approaches.

One of PennyLane’s key contributions is enabling researchers to compare QDNNs and CDNNs on the same problems. Since PennyLane allows hybrid quantum-classical models, users can train CDNNs and QDNNs on identical datasets, providing insights into their relative performance. Although quantum supremacy in deep learning is still an open question, early results suggest that QDNNs could offer advantages in feature extraction, kernel-based learning, and generative modeling, particularly for problems with complex high-dimensional structure.

By simulating quantum networks on classical hardware today, PennyLane provides a crucial testbed for develop-

ing quantum-enhanced deep learning architectures. As quantum technology progresses, these simulations will transition to real quantum processors, unlocking new possibilities for machine learning and data processing. For now, QDNNs remain an experimental but promising approach, representing a step toward harnessing the full potential of quantum computing for artificial intelligence.

#### IV. QUANTUM CLASSIFICATION

To better understand the differences in a quantum architecture and a classical one, let us consider a basic classifier DNN. In the simplest case, the architecture can be a basic feedforward single hidden layer classifier designed for binary classification tasks, where the input consists of a set of numerical features, lets chose eight for this example. It operates through two fully connected layers: the first projects the input into an eight-dimensional space and applies a rectified linear activation function to introduce nonlinearity, enhancing its ability to capture complex patterns. The second layer reduces the dimensionality to a single output, applying a sigmoid activation function to constrain the result within a probability range suitable for classification. This type of model learns by adjusting its internal parameters through gradient-based optimization techniques, typically using methods like stochastic gradient descent or adaptive moment estimation, minimizing a binary cross-entropy loss function. Its compact design makes it computationally efficient and effective for structured data classification tasks that require mapping numerical inputs to distinct categories based on learned patterns.

The neural network is structured to process an 8-dimensional input feature vector, transforming it through a series of weighted linear operations and nonlinear activations to produce a scalar output. The architecture begins with an input layer that accepts the feature vector  $x \in \mathbb{R}^8$ , which is then processed by a fully connected hidden layer. This hidden layer applies a linear transformation using a weight matrix  $W_1 \in \mathbb{R}^{8 \times 8}$  and a bias vector  $b_1 \in \mathbb{R}^8$ . The result of this linear operation is then passed through a ReLU activation function, which introduces nonlinearity to the model. This step can be expressed as:

$$h = \text{ReLU}(W_1x + b_1),$$

where the ReLU function operates element-wise and is defined as:

$$\text{ReLU}(z) = \max(0, z).$$

This activation ensures that only positive values are propagated while setting negative values to zero, enabling the network to learn complex representations while maintaining computational efficiency.

The activated hidden representation  $h$  is subsequently processed by the output layer, which consists of another fully connected transformation. This layer applies a weight matrix  $W_2 \in \mathbb{R}^{8 \times 1}$  and a scalar bias term  $b_2$  to produce the final output. The computation at this stage is given by:

$$y = \sigma(W_2h + b_2),$$

where the function  $\sigma(x)$  is the sigmoid activation, defined as:

$$\sigma(x) = \frac{1}{1 + e^{-x}}.$$

The sigmoid function maps the output to a range between 0 and 1, making it particularly well-suited for binary classification tasks. The final scalar value  $y$  can be interpreted as the probability of belonging to a particular class, allowing for meaningful decision-making based on the network's learned representations. This structured approach, combining linear transformations with nonlinear activations, enables the model to capture complex relationships within the input data while maintaining interpretability and stability in its predictions.

To construct a similar architecture for a QDNN we need to use quantum perceptrons, where each layer is defined by unitary matrices that evolve quantum states. Instead of weighted sums and nonlinear activations, quantum perceptrons use unitary transformations applied to qubits.

QDNNs can process and classify data in ways that CDNNs cannot. The architecture of a QDNN follows a structured approach, beginning with the encoding of classical data into quantum states, followed by a sequence of parameterized unitary transformations, and concluding with quantum measurement to derive the final classification decision.

A typical QDNN starts with a set of input qubits, which encode classical data into a quantum state. In this example, the network utilizes three input qubits, each representing a transformed version of classical data points. The core of the network consists of multiple hidden layers, where each layer applies parameterized unitary transformations. These unitary transformations serve as the quantum equivalent of weight matrices in CDNNs, allowing the system to evolve the quantum state in a structured and trainable manner. Finally, the last layer of the QDNN extracts useful information through quantum measurement, with a single-qubit measurement providing the classification outcome.

Before classical data can be processed within a QDNN, it must first be encoded into a quantum state. Given a classical input  $x$ , the encoding process maps the data into a quantum state representation. This transformation ensures that the network can operate within the quantum mechanical framework, leveraging the unique properties



of quantum computation such as superposition and entanglement.

The core computational power of a QDNN lies in its quantum perceptron layers. Each layer applies a unitary transformation  $U$  to the quantum state, modifying it while preserving coherence. The evolution of the quantum state follows the transformation,  $|\psi'\rangle = U|\psi\rangle$ .

where  $U$  is a unitary matrix satisfying the condition  $U^\dagger U = I$ , ensuring that the transformation remains reversible. Unlike classical networks, which rely on weight matrices and biases, the QDNN utilizes these unitary operations to manipulate quantum states without losing quantum information.

The architecture incorporates randomized unitary matrices, generated specifically for each perceptron. These transformations act across multiple qubits, introducing quantum correlations that enhance the network's computational capacity beyond classical architectures. Entanglement plays a fundamental role in this process, enabling a form of information encoding and manipulation that is fundamentally different from classical neural networks.

In a multi-qubit system, transformations must be properly structured to maintain coherence and ensure correct processing. Each unitary transformation in a QDNN is tensored with the identity matrix when applied to multiple qubits, ensuring that transformations operate within the appropriate Hilbert space. Mathematically, this is expressed as  $U_{\text{layer}} = U_{\text{qubit}} \otimes I$ .

This tensoring process ensures that unitary transformations are correctly applied in the quantum circuit without disrupting the overall structure of the network. Additionally, swapped operations are implemented to maintain proper qubit ordering within the layered transformations, further reinforcing the structural integrity of the quantum network.

Once the quantum state has evolved through the network's hidden layers, the final step is to extract a classification decision from the quantum system. This is achieved through a measurement operation, where an observable  $O$ , such as the Pauli-Z expectation value, is used to collapse the quantum state into a classical probability. The measurement process follows,  $\langle O \rangle = \langle \psi_{\text{final}} | O | \psi_{\text{final}} \rangle$ .

The extracted expectation value serves as the output of the QDNN, which is then mapped to a binary outcome for classification. This final measurement is a critical component of quantum machine learning, as it translates quantum state information back into a form that can be interpreted in the classical world.

QDNNs offer a novel approach to deep learning by harnessing quantum mechanical principles such as unitary evolution, entanglement, and measurement-based classification. While structurally similar to CDNNs in terms of layered transformations, the use of quantum perceptrons, tensoring, and quantum measurement introduces new computational advantages that are not present in classical architectures. As quantum computing technology advances, QDNNs may become a powerful tool for

solving problems that are intractable for classical machine learning models.

CDNNs and QDNNs share fundamental mathematical structures while exhibiting key differences due to their respective foundations in classical and quantum mechanics. One major distinction lies in the nature of transformations. In CDNNs, transformations are affine, expressed as  $h = Wx + b$ , whereas in QDNNs, transformations are unitary, evolving quantum states as  $|\psi'\rangle = U|\psi\rangle$ . This difference reflects the constraint that quantum evolution must preserve coherence, a property absent in classical networks. Another significant difference is the source of nonlinearity. CDNNs explicitly incorporate nonlinear activation functions such as ReLU and Sigmoid, enabling the network to model complex patterns. In contrast, QDNNs rely on measurement-induced nonlinearity since quantum evolution itself is inherently linear.

The way these networks process information also diverges in terms of state evolution. CDNNs compute outputs through matrix-vector multiplication, maintaining a straightforward relationship between inputs and learned weight matrices. QDNNs, however, evolve quantum states via unitary operations, which not only preserve quantum coherence but also allow for quantum superposition and entanglement. Despite these differences, both architectures rely on trainable parameters to optimize performance. In CDNNs, optimization targets the weight matrices  $W$  and biases  $b$ , while QDNNs optimize unitary transformations  $U$  using parameterized quantum gates.

Another distinction arises in the methods of gradient computation. CDNNs employ backpropagation, leveraging the chain rule of differentiation to update weights efficiently. QDNNs, on the other hand, use the parameter shift rule, which calculates gradients based on evaluating the function at shifted parameter values  $d\langle Z \rangle / d\theta$ .

Finally, a critical difference between CDNNs and QDNNs lies in their dimensionality. CDNNs operate in an  $n$ -dimensional Euclidean space, where input data and transformations are restricted to linear algebra over real or complex numbers. In contrast, QDNNs function within a  $2^n$ -dimensional Hilbert space, providing a vastly richer function representation due to the exponential scaling of quantum state space. This higher-dimensional representation enables QDNNs to potentially capture intricate patterns and correlations more efficiently than their classical counterparts. Despite these fundamental differences, both CDNNs and QDNNs share the goal of learning input-output mappings, albeit within distinct mathematical frameworks.

CDNNs and QDNNs share structural similarities, both consisting of layered transformations, trainable parameters, and optimization via gradient descent. However, QDNNs introduce quantum properties such as entanglement, superposition, and exponentially large state spaces, making them potentially more expressive than CDNNs.

While CDNNs rely on nonlinear activation functions,

QDNNs achieve equivalent effects through quantum measurement and entanglement-induced correlations. The primary difference is that classical networks use weight matrices, whereas quantum networks use unitary operators.

Training in QDNNs is fundamentally different due to the unitary constraint and the parameter shift rule, which replaces traditional backpropagation. Additionally, QDNNs encode data differently, using quantum states rather than real-valued vectors, leading to computational advantages for problems with high-dimensional correlations.

Ultimately, the choice between CDNNs and QDNNs depends on the problem domain. While CDNNs are well-suited for classical data, QDNNs may offer superior performance in tasks where quantum correlations and high-dimensional state representations are advantageous, such as quantum chemistry, material science, and certain machine learning tasks that exploit quantum features.

### A. Quantum Classification Example

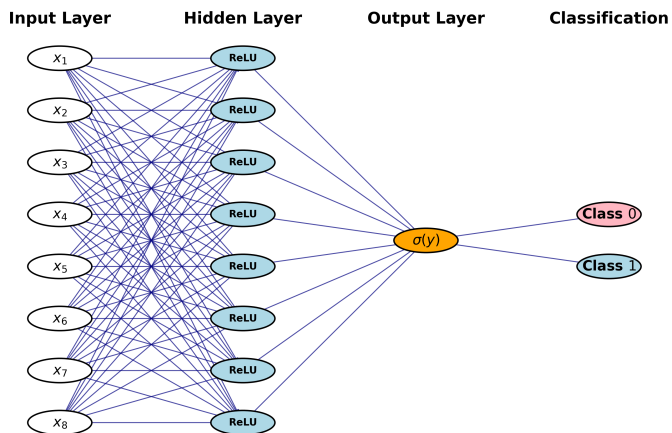


FIG. 1: A schematic representation of a CDNN architecture for binary classification. The input layer consists of 8 features  $x_i$ , which are processed through a hidden layer of 8 neurons with ReLU activation. The final output layer consists of a single neuron with a sigmoid activation function  $\sigma(y)$ , producing a probability score that determines classification into either Class 0 or Class 1.

Classification data comes in pairs  $\{X, y\}$ , where  $X$  is a vector of  $n$  input features and  $y$  is the target value 0 or 1. The CDNN used has an architecture of  $n$  inputs, a layer of 8 hidden perceptrons, and an output perceptron. A binary cross entropy loss function and the Adam optimization algorithm are used. When classifying, 100 epochs are used for training the CDNN.

In QDNNs, it is common to structure the number of nodes in hidden layers as  $\log_2(N)$ , where  $N$  is the num-

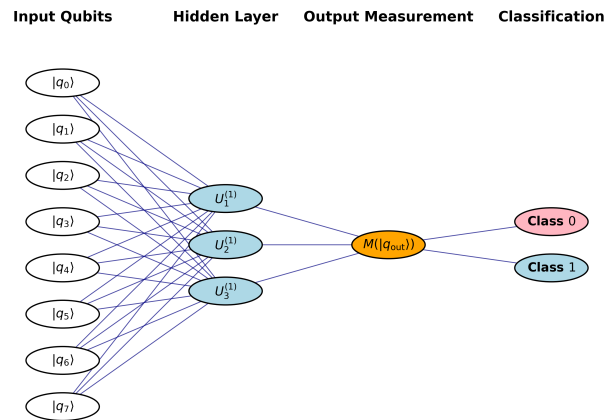


FIG. 2: A schematic representation of a QDNN architecture. The input layer consists of 8 qubits  $|q_i\rangle$ , which are processed through a hidden layer of quantum perceptrons  $U_i^{(1)}$ . The final output measurement  $M(|q_{out}\rangle)$  determines the classification, assigning the input to either Class 0 or Class 1. The connections represent quantum operations applied between layers.

ber of input variables. This choice is rooted in both quantum computational efficiency and the way quantum systems encode information. In quantum computing, a system with  $n$  qubits can represent  $2^n$  states simultaneously due to quantum superposition. To process  $N$  classical input variables efficiently, the natural mapping is to use  $\log_2(N)$  qubits, ensuring that quantum operations scale optimally without redundancy. Additionally, quantum circuits operate using unitary transformations, and a well-structured quantum neural network should minimize circuit depth. Using  $\log_2(N)$  nodes in hidden layers maintains an optimal depth-to-width ratio, allowing for efficient parameterization with quantum gates. Many quantum algorithms, such as the Quantum Fourier Transform (QFT) and variational quantum circuits, follow a similar log-scaled structure to ensure logarithmic circuit depth.

Another key reason for this design choice is the role of entanglement in representing feature correlations. Quantum neural networks rely on entanglement to capture dependencies between input variables, and a logarithmic number of nodes allows for efficient encoding and manipulation of these relationships. Using more nodes than necessary introduces redundant parameterization, while too few nodes can limit the network's ability to learn complex correlations. Additionally, quantum computing offers advantages in compression and speedup compared to classical deep learning architectures. Classical neural networks often require deep layers to capture intricate patterns, but quantum networks, leveraging Hilbert space representations, can encode complex functions with significantly fewer parameters. A logarithmic scaling of hidden nodes ensures efficient quantum learning while maintaining computational feasibility.

Furthermore, in quantum machine learning (QML), feature encoding in a Hilbert space often relies on unitary transformations that act on  $\log_2(N)$  qubits. Many QML architectures, such as quantum variational classifiers, follow this log-scaled structure to ensure an efficient transformation of input features. This approach aligns with the fundamental principles of quantum computation by optimizing the mapping of classical data into a quantum system, reducing circuit depth, leveraging quantum entanglement, and allowing for quantum speedup. The use of  $\log_2(N)$  nodes in hidden layers is therefore a natural and effective design choice in quantum neural networks.

The classification pair  $\{X, y\}$  is converted into the form  $\{|\phi^{\text{in}}\rangle, |\phi^{\text{target}}\rangle\}$  for the QDNN. This is done by converting an  $n$ -dimensional input vector  $X$  into a  $\log_2 n$ -qubit state. Specifically, some input vector

$$X = \begin{pmatrix} x_1 \\ x_2 \\ \vdots \\ x_n \end{pmatrix}, \quad (18)$$

is converted into an  $n$ -dimensional quantum state  $|\phi^{\text{in}}\rangle$  of the form

$$|\phi^{\text{in}}\rangle = \frac{x_1|00\dots 0\rangle + x_2|00\dots 1\rangle + \dots + x_n|11\dots 1\rangle}{\sqrt{x_1^2 + x_2^2 + \dots + x_n^2}}. \quad (19)$$

The target value  $y = 0$  is converted to the target state  $|\phi^{\text{target}}\rangle = |0\rangle$ , and the target value  $y = 1$  is converted to the target value  $|\phi^{\text{target}}\rangle = |1\rangle$ . To mirror the CDNN architecture, the QDNN architecture is set to  $\log_2 n$  input qubits, a layer of 3 hidden quantum perceptrons, and an output quantum perceptron. When classifying, 25 epochs are used for training the QDNN.

Considering output values of 1 to be ‘‘positive’’ and output values of 0 to be ‘‘negative,’’ classification efficiency is measured to be the average of the true positive rate, true negative rate, and accuracy.

We generate two types of classification data: 1 function data and 3 function data. 1 function signal data ( $y = 1$ ) is first generated by sampling each input feature  $x_i$  from a normal distribution with a mean of 1.0 and a standard deviation of 0.5:

$$x_i \sim \mathcal{N}(1.0, 0.5^2). \quad (20)$$

Then, to introduce correlations, each feature  $x_i$  is updated based on the other features  $x_j$  (with  $i \neq j$ ) using the transformation:

$$x_i \leftarrow x_i + 0.1 \sin(\pi x_j) + \epsilon, \quad (21)$$

where  $\epsilon \sim \mathcal{N}(0.0, \sigma^2)$  and  $\sigma$  is a noise parameter. Similarly, 1 function background data ( $y = 0$ ) is generated with a normal distribution

$$x_i \sim \mathcal{N}(0.0, 1.0^2), \quad (22)$$

then is transformed using

$$x_i \leftarrow x_i + 0.1 \cos(\pi x_j) + \epsilon. \quad (23)$$

3 function signal data and background data are also initially drawn from Eqs. (20) and (22), respectively, but undergo three complex transformations instead of one. Specifically, signal data is transformed with

$$\begin{aligned} x_i &\leftarrow x_i + 0.1 \sin^2(\pi x_j) + \epsilon_1 \\ x_i &\leftarrow x_i + 0.1 \log^2(|x_j| + 1) + \epsilon_2 \\ x_i &\leftarrow x_i + 0.1 e^{-|x_j|} + \epsilon_3, \end{aligned} \quad (24)$$

and background data is transformed with

$$\begin{aligned} x_i &\leftarrow x_i + 0.1 \cos^2(\pi x_j) + \epsilon_1 \\ x_i &\leftarrow x_i + 0.1 \tan^2(x_j) + \epsilon_2 \\ x_i &\leftarrow x_i + 0.1 e^{-|x_j|} + \epsilon_3, \end{aligned} \quad (25)$$

where  $\epsilon_1, \epsilon_2, \epsilon_3 \sim \mathcal{N}(0.0, \sigma^2)$ .

Although QDNNs outperform CDNNs in practically all cases, the factors that seem to play the most critical roles in QDNN outperformance are the number of training pairs, the complexity of the data, and the number of input variables. To optimize data generation for the QDNN outperforming the CDNN, the data complexity and the number of input variables should be high, and the number of training pairs should be low.

When decreasing the number of training pairs, both DNNs decrease in accuracy as expected, but the QDNN outperforms the CDNN significantly more. Considering 3 function data with  $0.05\sigma$  noise level, 8 input features, and 500 training pairs yields a classical classification efficiency of 0.6436 and a quantum classification efficiency of 0.8745, but decreasing the number of training pairs to 50 yields a classical classification efficiency of 0.4716 and a quantum classification efficiency of 0.8116. By decreasing the number of training pairs by a factor of 10, the quantum classification efficiency to classical classification efficiency ratio increases by 27%.

When increasing the complexity of the data, both DNNs decrease in accuracy as expected, but the QDNN outperforms more. Considering data with  $0.05\sigma$  noise level, 8 input features, and 250 training pairs, using the 1 function generation yields a classical classification efficiency of 0.8378 and a quantum classification efficiency of 0.9678, but increasing to 3 function generation yields a classical classification efficiency of 0.6290 and a quantum classification efficiency of 0.8704. By increasing the complexity of the data by a factor of 3, the quantum classification efficiency to classical classification efficiency ratio increases by 20%.

When increasing the number of input features, the CDNN decreases in accuracy, but the QDNN increases in accuracy. Again, the QDNN consistently outperforms. Considering 3 function data with  $0.05\sigma$  noise level, and 250 training pairs, using 8 input features yields a classical

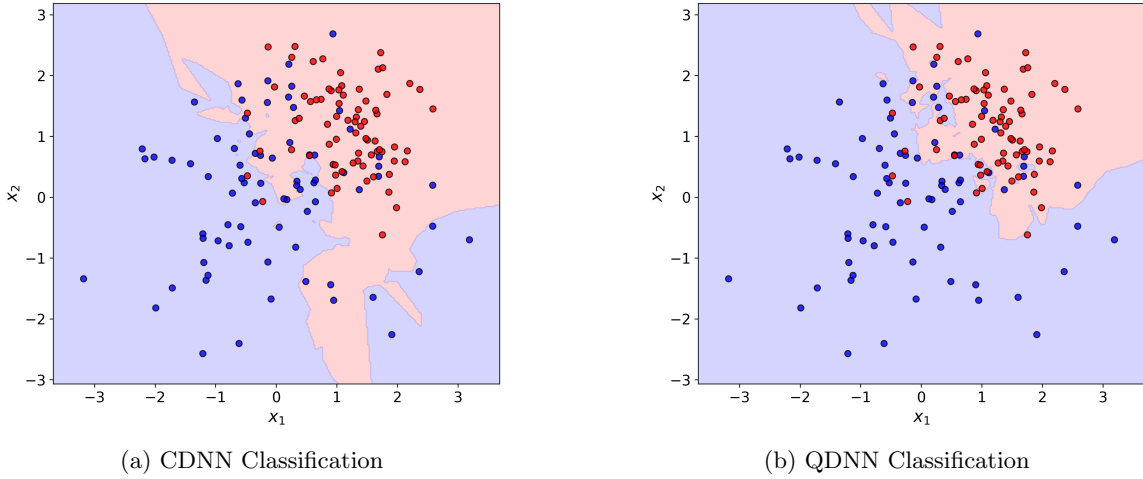


FIG. 3: Classification comparison of 1 function data, generated by Eqs. (20)-(23) with  $0.2\sigma$  noise level, and 8 input features. Two of the eight input features are plotted, with signal points in red and background points in blue. The QDNN outperforms the CDNN in classification accuracy.

classification efficiency of 0.6290 and a quantum classification efficiency of 0.8704, but increasing the number of input features to 16 yields a classical classification efficiency of 0.5327 and a quantum classification efficiency of 0.9359. By increasing the number of variables by a factor of 2, the quantum classification efficiency to classical classification efficiency ratio increases by 27%.

Noise plays a role in QDNN outperformance, but not a significant one. When decreasing the amount of noise in the data, both DNNs increase in accuracy as expected, but the QDNN outperforms more. Considering 1 function data with 8 input features and 250 training pairs data, setting the noise level to  $0.2\sigma$  yields a classical classification efficiency of 0.7917 and a quantum classification efficiency of 0.8704, but decreasing the noise level to  $0.05\sigma$  yields a classical classification efficiency of 0.8378 and a quantum classification efficiency of 0.9678. By decreasing the amount of noise by a factor of 4, the quantum classification efficiency to classical classification efficiency ratio increases by 5%.

## V. QUANTUM REGRESSION

As another preliminary comparison, we perform some basic regression tests on a CDNN and QDNN. To do this, we generate data sets by plugging 100 evenly distributed values  $x_i \in [-2, 4]$  into the following target functions

with varying complexity:

$$y = \cos 4x \quad (26)$$

$$y = \sin x^3 + \cos 2x^2 + \sin 4x \quad (27)$$

$$y = \sin 5x^3 + \cos 10x^2 + \sin 20x \quad (28)$$

$$y = \sin(x^3 + 5 \sin 2x) \quad (29)$$

$$+ \cos(2x^2 + 3 \cos x) + \sin(4x + \cos 3x)$$

$$y = \sin e^x + \cos e^{2x} + \sin e^{3x} \quad (30)$$

$$y = \sin(\pi x) \cos(\pi \sin x^2) + \sin(\pi \cos x^2). \quad (31)$$

Then, we introduce some noise in the data with the transformation

$$y_i \leftarrow y_i + \mathcal{N}(0.0, \sigma^2), \quad (32)$$

where the standard deviation  $\sigma$  takes the values  $\sigma = 0.1, 0.25, 1.0$  for each of the six target functions. This gives us 15 sets of 100 noisy data points  $(x_i, y_i)$  on which we perform a regression with the CDNN and QDNN. Some example fits are shown in Figs. 4 and 5.

To judge the quality of a given DNN fit, we use a simple regression metric  $M_{\text{reg}}$  defined by

$$M_{\text{reg}} = \frac{\int_{x_{\min}}^{x_{\max}} |y_{\text{DNN}}(x) - y_{\text{true}}(x)| dx}{\left| \int_{x_{\min}}^{x_{\max}} y_{\text{true}}(x) \right|}. \quad (33)$$

Here, a value of  $M_{\text{reg}} = 0$  indicates a perfect fit. Some values of  $M_{\text{reg}}$  for both the CDNN and QDNN are displayed in Tables IX-XIV. Using these metric values, we calculate the quantum outperformance  $\Xi$  for a given data set and number of epochs by

$$\Xi = M_{\text{reg}}^{\text{CDNN}} / M_{\text{reg}}^{\text{QDNN}} - 1. \quad (34)$$

Therefore,  $\Xi > 0$  indicates that the QDNN outperforms, and  $\Xi < 0$  indicates the CDNN outperforms. The mag-

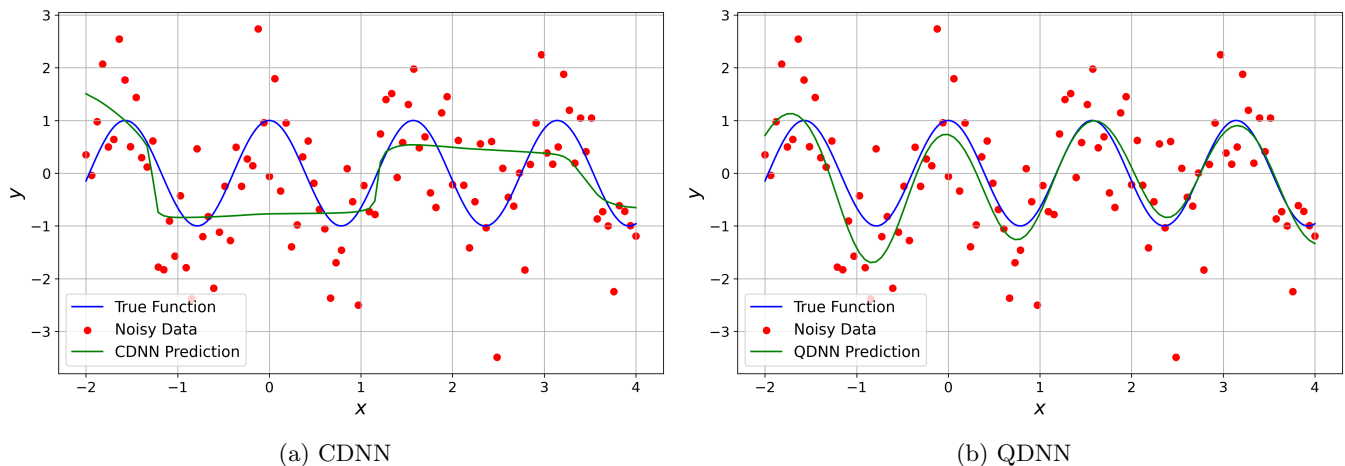


FIG. 4: A function regression comparison between a) CDNN and b) QDNN using target Function Eq. (26), with  $1\sigma$  noise level, and trained using 50 epochs.

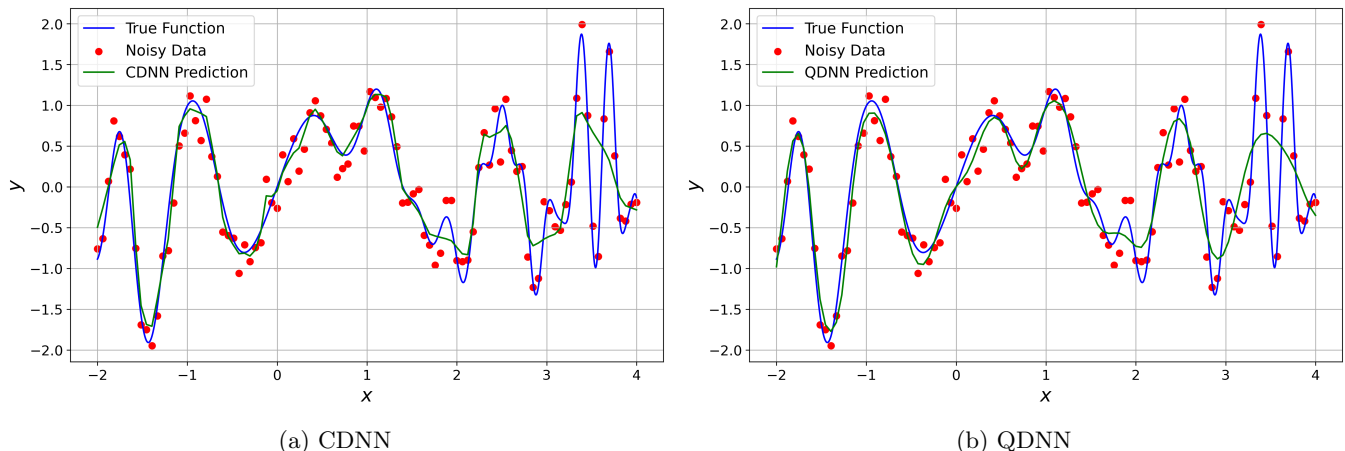


FIG. 5: A function regression comparison between a) CDNN and b) QDNN using target Function Eq. (31), with  $0.25\sigma$  noise level, and trained using 250 epochs.

nitude of  $\Xi$  indicates the extent to which the better DNN outperforms.

The development of QDNNs has introduced new possibilities for achieving computational advantages over CDNNs in various applications. To systematically assess and quantify these advantages, a variety of complexity and information-theoretic metrics—originally developed for classical systems—can be repurposed in the quantum context. Among these, Nonlinearity, Frequency Complexity, Fractal Dimension, Mutual Information, and Fourier Transform Complexity have emerged as particularly insightful.

Nonlinearity measures the deviation of a dataset from a linear trend and can reveal the expressive power of a model in capturing nonlinear relationships. In the quantum setting, parameterized quantum circuits have been shown to exhibit enhanced nonlinear representational capacity. Du *et al.* demonstrate that QDNNs possess a richer functional landscape than classical models due to

quantum operations that naturally induce nonlinearity [18]. This implies that datasets exhibiting high nonlinearity may be more efficiently modeled by QDNNs, making the nonlinearity metric a useful indicator of potential quantum advantage.

Frequency Complexity, which counts the number of local maxima in a signal’s power spectrum, provides insight into the oscillatory structure and richness of data representations. The Quantum Fourier Convolutional Neural Network proposed by Shen and Liu shows that QDNNs leveraging quantum Fourier transforms can outperform classical CNNs in frequency-domain processing [19]. The exponential speed-up in extracting and interpreting frequency components underscores the utility of frequency complexity as a tool for identifying cases where QDNNs may offer significant advantages.

While the Fractal Dimension is less commonly applied in direct QDNN benchmarking, it serves as a proxy for structural complexity. Verdon *et al.* discuss how

TABLE I: Parameters for the double-summation expression of  $\hat{\Xi}$  from equation 43.

Coefficient	Value	Variable $X_j$	Power of $n$
$\alpha$	0.0101	exp. prefactor	—
$\beta_{10}$	-1.17	$\mathfrak{N} - 0.25$	$n^0$
$\beta_{11}$	0.0163	$\mathfrak{N} - 0.25$	$n^1$
$\beta_{12}$	$-2.65 \times 10^{-5}$	$\mathfrak{N} - 0.25$	$n^2$
$\beta_{20}$	-0.0222	$\Phi - 24.5$	$n^0$
$\beta_{21}$	$2.82 \times 10^{-4}$	$\Phi - 24.5$	$n^1$
$\beta_{22}$	$-1.40 \times 10^{-6}$	$\Phi - 24.5$	$n^2$
$\beta_{23}$	$3.33 \times 10^{-9}$	$\Phi - 24.5$	$n^3$
$\beta_{24}$	$-3.14 \times 10^{-12}$	$\Phi - 24.5$	$n^4$
$\beta_{30}$	-1.10	$\mathfrak{D} - 0.95$	$n^0$
$\beta_{31}$	$5.39 \times 10^{-3}$	$\mathfrak{D} - 0.95$	$n^1$
$\beta_{32}$	$-9.88 \times 10^{-6}$	$\mathfrak{D} - 0.95$	$n^2$
$\beta_{33}$	$7.96 \times 10^{-9}$	$\mathfrak{D} - 0.95$	$n^3$
$\beta_{34}$	$-4.06 \times 10^{-12}$	$\mathfrak{D} - 0.95$	$n^4$
$\beta_{40}$	0.548	$\mathfrak{M} + 0.05$	$n^0$
$\beta_{41}$	$-6.57 \times 10^{-3}$	$\mathfrak{M} + 0.05$	$n^1$
$\beta_{42}$	$3.05 \times 10^{-5}$	$\mathfrak{M} + 0.05$	$n^2$
$\beta_{43}$	$-6.81 \times 10^{-8}$	$\mathfrak{M} + 0.05$	$n^3$
$\beta_{44}$	$6.05 \times 10^{-11}$	$\mathfrak{M} + 0.05$	$n^4$
$\beta_{50}$	$-5.97 \times 10^{-7}$	$\mathfrak{F} - 4999.5$	$n^0$
$\beta_{51}$	$-1.48 \times 10^{-8}$	$\mathfrak{F} - 4999.5$	$n^1$
$\beta_{52}$	$2.27 \times 10^{-11}$	$\mathfrak{F} - 4999.5$	$n^2$
$\beta_{53}$	$-2.39 \times 10^{-14}$	$\mathfrak{F} - 4999.5$	$n^3$
$\beta_{54}$	$2.03 \times 10^{-17}$	$\mathfrak{F} - 4999.5$	$n^4$

quantum neural architectures can more efficiently model highly structured sequences that exhibit self-similar or hierarchical properties—traits often captured by high fractal dimension [20]. Thus, this metric can be applied to characterize tasks where QDNNs offer improved performance through their natural alignment with high-dimensional, complex data manifolds.

Mutual Information quantifies the amount of information shared between input and output variables and is an established metric for evaluating the information retention capacity of neural networks. Chen *et al.* conduct a comparative study of QDNNs and CDNNs, showing that quantum models often preserve and utilize mutual information more effectively due to entanglement and superposition [21]. Therefore, mutual information serves not only as a metric of model performance but also as a diagnostic tool for identifying scenarios in which quantum information processing offers clear benefits.

Lastly, Fourier Transform Complexity, defined as the total energy contained in the frequency domain, reflects the signal richness and processing capacity of a model. In the context of high-energy physics, Wetzal and Scherzer demonstrate that Quantum Convolutional Neural Networks (QCNNs) trained on event classification tasks outperform classical CNNs by leveraging their superior frequency-domain analysis capabilities [22]. This validates the Fourier complexity metric as a relevant benchmark for comparing quantum and classical architectures,

particularly for tasks with substantial spectral content.

Together, these metrics offer a multidimensional framework for understanding when and why QDNNs may outperform classical models. They provide a principled way to diagnose task complexity, model capacity, and potential quantum advantage. These metrics can be used to construct a composite quantum qualifier  $\hat{\Xi}$  that can be used to estimate quantum outperformance  $\Xi$  based purely on characteristics of the data. Specifically, we examined five different function characteristics, namely, nonlinearity ( $\mathfrak{N}$ ), frequency complexity ( $\Phi$ ), fractal dimension ( $\mathfrak{D}$ ), mutual information ( $\mathfrak{M}$ ), and Fourier transform complexity ( $\mathfrak{F}$ ), for correlations with quantum outperformance  $\Xi$ . For each of these function qualities we explicitly define how we calculate each as follows.

Nonlinearity [23] ( $\mathfrak{N}$ ) quantifies how much some dataset  $(x_i, y_i)$  deviates from linear behavior. To compute it, we first perform a linear regression on the set of data points  $(x_i, y_i)$ , which yields points  $(x_i, \hat{y}_i^{\text{lin}})$ . Then, the nonlinearity metric is defined to be the ratio between the residual sum of squares of the linear fit and the residual sum of squares from the mean:

$$\mathfrak{N} = \frac{\sum_{i=1}^n (y_i - \hat{y}_i^{\text{lin}})^2}{\sum_{i=1}^n (y_i - \bar{y})^2}, \quad (35)$$

where

$$\bar{y} = \frac{1}{n} \sum_{i=1}^n y_i. \quad (36)$$

Values of  $\mathfrak{N}$  near 0 indicate the data is well-approximated by a linear model, while values closer to 1 suggest higher nonlinearity.

Frequency complexity [24] ( $\Phi$ ) measures the richness of the dataset’s structure in the frequency domain. To compute it, we first perform a discrete Fourier transform on the set of  $y$  values:  $y \xrightarrow{\mathcal{F}} \hat{y}$ . Letting  $\hat{y}_k$  denote the  $k$ th Fourier coefficient, we compute the dataset’s power spectrum:  $P_k = |\hat{y}_k|^2$ , which represents the contribution of each frequency component. The frequency complexity is defined as the number of local maxima (peaks) in the power spectrum:

$$\Phi = |\{k \mid P_k \text{ is a local maximum}\}|. \quad (37)$$

A higher value indicates that the dataset contains a greater number of distinct frequency components, reflecting increased structural or oscillatory complexity.

Fractal dimension [25] ( $\mathfrak{D}$ ) quantifies the detailed complexity or roughness of the dataset. Here, we compute the box-counting dimension of the data points. We first choose a logarithmically spaced series of box sizes  $s_k$  from 1 to  $N$ , the number of data points. Then, for each box size  $s_k$ , we partition the set of  $y$  values into non-overlapping segments of size  $s_k$  and take a normalized sum over the range of the  $y$  values within each segment:

$$C(s_k) = \frac{1}{s_k} \sum_{i=0}^{\lfloor N/s_k \rfloor - 1} (\max(y_{is_k}, y_{i s_k + 1}, \dots, y_{(i+1)s_k - 1}) - \min(y_{is_k}, y_{i s_k + 1}, \dots, y_{(i+1)s_k - 1})). \quad (38)$$

Finally, we perform a linear regression on  $\log C(s_k)$  against  $\log s_k$ , yielding

$$\log C(s_k) = -\mathfrak{D} \log s_k + \text{const.} \quad (39)$$

The negative slope  $\mathfrak{D}$  is the fractal dimension, where a higher value of  $\mathfrak{D}$  indicates a more complex or rough structure.

Mutual information [26] ( $\mathfrak{M}$ ) is a measure of the amount of information that one variable provides about another. It quantifies the reduction in uncertainty of one variable due to the knowledge of the other. In general, the mutual information between two variables  $X$  and  $Y$  is defined as:

$$I(X; Y) = H(X) + H(Y) - H(X, Y), \quad (40)$$

where  $H(X)$  and  $H(Y)$  are the entropies of  $X$  and  $Y$ , respectively, and  $H(X, Y)$  is the joint entropy of  $X$  and  $Y$ . The entropy of a variable is a measure of uncertainty, while the joint entropy captures the uncertainty in the combined system of  $X$  and  $Y$ . Here, mutual information is computed using a contingency table, which represents the joint probability distribution of the two variables. For our given set of data points  $(x_i, y_i)$ , we first compute their 2D histogram, which gives the joint distribution of  $x$  and  $y$ . The mutual information is then calculated by summing over all possible pairs of values  $(x_i, y_j)$  in the contingency table as follows:

$$\mathfrak{M} = \sum_{i,j} \frac{n_{ij}}{N} \log \left( \frac{n_{ij}/N}{\left(\sum_i n_{ij}/N\right) \left(\sum_j n_{ij}/N\right)} \right), \quad (41)$$

where  $n_{ij}$  represents the count in the  $(i, j)$ -th cell of the 2D histogram, and  $N$  is the total number of data points. This formula evaluates how much knowing one variable reduces the uncertainty about the other by considering their joint distribution and the marginal distributions of each variable.

Finally, Fourier transform complexity [27] ( $\mathfrak{F}$ ) assesses the complexity or variability of the dataset's structure in the frequency domain and is computed through a process similar to the frequency complexity ( $\Phi$ ). Specifically, we perform a discrete Fourier transform on the set of  $y$  values and compute the power spectrum:  $P_k = |\hat{y}_k|^2$ . The Fourier transform complexity is defined as the sum of the power spectrum:

$$\mathfrak{F} = \sum_k P_k. \quad (42)$$

A higher  $\mathfrak{F}$  indicates that the data has a greater amount of variability as it progresses in the domain.

In Tables VI-VIII, we show the values of these five function characteristics for each of the target functions. We then use Eq. (34) to calculate the quantum outperformance  $\Xi$  for each of the tests, and we plot the values of  $\Xi$  for a given number of epochs against each of the five function characteristics. We perform linear regressions on this and display the results in Tables XV and XVI. This indicates the correlation between quantum outperformance and the characteristics of the target function data for a given number of epochs. Using this information, we fit polynomial curves (and an exponential curve for  $\mathfrak{N}$ ) to the regression slopes and  $R^2$  values as a function of the number of epochs. Since the polynomial fit of the regression slopes against the number of epochs approximates the correlation between quantum outperformance  $\Xi$  and a given function characteristic, we construct a linear function corresponding to this correlation for a given number of epochs. Finally, we define the quantum qualifier  $\hat{\Xi}$  by summing all of these linear functions (with slope given by the  $\Xi$  regression slope polynomial fit) and then weighting by the strength of the correlation (given by the  $R^2$  polynomial fit):

$$\hat{\Xi} = e^{-\alpha n} \sum_{i=0}^2 \beta_{1i} n^i X_1 + \sum_{j=2}^5 \sum_{i=0}^4 \beta_{ji} n^i X_j. \quad (43)$$

This quantum qualifier can estimate the value of  $\Xi$  based on the five function characteristics and the number of epochs  $n$  that the CDNN and QDNN are trained on. Here, the coefficients are parameterized in one indexed set  $\beta_{ji}$ , where  $j$  indexes the corresponding observable  $X_j$ :

$$X_j \in \{\mathfrak{N}-0.25, \Phi-24.5, \mathfrak{D}-0.95, \mathfrak{M}+0.05, \mathfrak{F}-4999.5\}. \quad (44)$$

Here, the exponential prefactor  $e^{-\alpha n}$  is included explicitly (with  $\alpha = 0.0101$ ), and parameters  $\beta_{ji}$  encode all coefficients.  $\alpha$  is a fixed scalar in the exponential. The outer sum  $j$  runs over different offset parameters ( $\mathfrak{N}, \Phi, \mathfrak{D}, \mathfrak{M}, \mathfrak{F}$ ), each scaled by a specific offset. The inner sum  $\sum_i$  runs over powers of  $n$ , representing polynomial dependence. Table I shows the numerical parameters of the quantum qualifier expression.

Equation (43) captures the main conclusions that are immediately evident from Tables XV and XVI; for example, that mutual information  $\mathfrak{M}$  has the most positive correlation with quantum outperformance, while fractal dimension  $\mathfrak{D}$  has the most negative and strongest correlation with quantum outperformance. However, the expression is cumbersome, so we would like to construct a simpler version of a quantum qualifier that serves as a quantified general rule. To do this, we will consider some target functions that use the same kinematic variables and CFFs as the relevant DVCS process to better

simulate the experimental data of interest.

## VI. DVCS REGRESSION QUANTUM QUALIFIER

To evaluate the potential for quantum advantage specifically in DVCS, we construct a quantum qualifier

$$F_1(\phi) = (\mathcal{E} \sin \phi + \mathcal{H} \cos \phi) e^{-x_B t} + (\tilde{\mathcal{E}} \sin 2\phi + \tilde{\mathcal{H}} \cos 2\phi) e^{-Q^2} \quad (45)$$

$$F_2(\phi) = (\mathcal{E} \sin(\phi + x_B t) + \mathcal{H} \cos(\phi - Q^2 x_B)) e^{-x_B t/Q^2} + (\tilde{\mathcal{E}} \sin(2\phi + t) + \tilde{\mathcal{H}} \cos(2\phi - x_B)) \frac{e^{-Q^2/t}}{10000} \quad (46)$$

$$F_3(\phi) = (\mathcal{E} \sin(3\phi + x_B t) + \mathcal{H} \cos(4\phi - Q^2 x_B)) e^{-x_B t/Q^2} + (\tilde{\mathcal{E}} \sin(5\phi + t) + \tilde{\mathcal{H}} \cos(6\phi - x_B)) \frac{e^{-Q^2/t}}{10000} \quad (47)$$

$$F_4(\phi) = (\mathcal{E} e^{\sin(\phi + x_B t)} + \mathcal{H} \log(1 + \cos(\phi - Q^2 x_B))) e^{-x_B t/Q^2} + (\tilde{\mathcal{E}} \sin(e^{2\phi + t}) + \tilde{\mathcal{H}} \cos(\ln(1 + 2\phi - x_B))) \frac{e^{-Q^2/t}}{10000} \quad (48)$$

where the kinematic variables are set to  $x_B = \{0.1, 0.2, 0.3\}$ ,  $t = \{-0.1, -0.2, -0.6\}$ ,  $Q^2 = 1.0$ , and the CFFs are set to  $\mathcal{E} = 0.5$ ,  $\mathcal{H} = 1.0$ ,  $\tilde{\mathcal{E}} = 0.3$ ,  $\tilde{\mathcal{H}} = 0.7$ . Data is generated by calculating the DVCS cross-section values for 24 evenly spaced values of  $\phi$  between 0 and  $2\pi$ .

Generating sets of data for the four DVCS cross-section functions for the three values of  $x_B$  and  $t$  gives us 36 data sets to perform a regression on using early-stopping classical and quantum DNNs. Performing a similar analysis as in the previous section, we found that two of these had significant correlations with  $\Xi_{DVCS}$ : non-linearity (negative) and mutual information (positive). Specifically, plotting these against  $\Xi_{DVCS}$  and performing linear regressions gave  $\Xi_{DVCS} = -2.9\mathfrak{N} + 2.19$  and  $\Xi_{DVCS} = 1.08\mathfrak{M} - 1.57$  with  $R^2$  values of 0.466 and 0.572, respectively.

Using this, we constructed a simple quantum qualifier that estimates whether a QDNN or CDNN will outperform based solely on  $\mathfrak{N}$  and  $\mathfrak{M}$ :

$$\hat{\Xi}_{DVCS} = 0.5\mathfrak{M} - 1.6\mathfrak{N} + 0.6. \quad (49)$$

Just as before,  $\hat{\Xi}_{DVCS} > 0$  indicates that a QDNN will outperform and vice versa, and the magnitude of  $\Xi$  approximates the extent to which the better DNN will outperform.

## VII. EXPERIMENTAL DATA AND PSEUDODATA GENERATION

This analysis utilizes DVCS experimental data from Hall A [17, 28, 29] and Hall B [30] at Jefferson Lab (JLab). The dataset, summarized in Table II, includes both helicity-independent and helicity-dependent cross-sections. However, our focus is exclusively on the

$\hat{\Xi}_{DVCS}$  for the regression of DVCS data. The purpose of this quantum qualifier is to determine whether a set of DVCS data will be better suited for regression by a classical or quantum DNN, where both DNNs perform at the optimal number of epochs. To construct the QQ, we use four DVCS cross-section functions to generate noisy data:

helicity-independent (unpolarized) cross-sections. The data is finely binned in a fourfold differential cross-section parameterized by  $Q^2$ ,  $x_B$ ,  $t$ , and  $\phi$ , comprising a total of 3,885 data points for analysis.

The dataset spans measurements from both the 6 GeV and 12 GeV JLab experimental programs. The 12 GeV data extend to higher values of  $Q^2$ , reaching up to 8.4 GeV<sup>2</sup>, while the 6 GeV-era data cover lower ranges. The majority of the data points originate from the e1-DVCS1 experiment at Hall B [30], which operated with a fixed beam energy of 5.75 GeV and probed a  $Q^2$  range from 1.0 to 4.6 GeV<sup>2</sup>. All experimental datasets used in this analysis are detailed in Table II.

### A. Pseudodata Generation

The pseudodata set was generated using the following *basic* model function:

$$G(x_B, t) = (ax_B^2 + bx_B) e^{ct^2 + dt + e} + f. \quad (50)$$

where  $G(x_B, t)$  represents the CFFs and DVCS cross-section components:  $\Re\mathcal{H}$ ,  $\Re\mathcal{E}$ ,  $\Re\tilde{\mathcal{H}}$ , and  $DVCS$ . The parameters  $\{a, b, c, d, e, f\}$  for each case are listed in Table III, and are based on initial tests. The structure of this model function allows for linear or non-linear changes in  $x_B$  with exponential flexibility in  $t$ . The parameterization has no physical meaning as the model is purely designed for testing the DNN extractions.

To compute the photon leptoproduction cross-section described in Section II, the CFFs are taken from the *basic* model. Within each kinematic bin, the cross-section is randomly sampled from a Gaussian distribution centered on the calculated value at each  $\phi$  point, with the



TABLE II: Summary of the DVCS data from JLAB used in this analysis. The table includes information on the data source and the kinematic range covered by the helicity-independent cross-section.

Experiment	Publication Year	$E_{beam}$ (GeV)	$Q^2$ (GeV $^2$ )	$-t$ (GeV $^2$ )	$x_B$	Number of Points
Hall A E12-06-114 [17]	2022	4.487 - 10.992	2.71 - 8.51	0.204 - 1.373	0.363 - 0.617	1080
Hall A E07-007 [28]	2017	3.355 - 5.55	1.49 - 2.	0.177 - 0.363	0.356 - 0.361	404
Hall A E00-110 [29]	2015	5.75	1.82 - 2.37	0.171 - 0.372	0.336 - 0.401	468
Hall B e1-DVCS1 [30]	2015	5.75	1.11 - 3.77	0.11 - 0.45	0.126 - 0.475	1933

TABLE III: The parameters used in Eq. (50) to generate the second pseudodata data set.

$CFFs$	$a$	$b$	$c$	$d$	$e$	$f$
$\Re\mathcal{H}$	-4.41	1.68	-9.14	-3.57	1.54	-1.37
$\Re\mathcal{E}$	144.56	149.99	0.32	-1.09	-148.49	-0.31
$\Re\tilde{\mathcal{H}}$	-1.86	1.50	-0.29	-1.33	0.46	-0.98
$DVCS$	0.50	-0.41	0.05	-0.25	0.55	0.166

standard deviation corresponding to experimental uncertainties. The generated kinematic settings and  $\phi$  points match those of the experimental data used in this study, ensuring that acceptance effects and statistical limitations are properly accounted for.

The uncertainties introduced in the pseudodata align with the reported experimental errors from JLab data [17, 28–30], which include both statistical and systematic contributions. As a result, the generated pseudodata closely replicate real-world experimental conditions that influence the measured cross-sections.

For each pseudodata set, replica data are generated by resampling the cross-section at the central value of each bin, using Gaussian sampling within the experimental uncertainties. This ensures a realistic representation of measurement fluctuations.

### VIII. PSEUDODATA REGRESSION

In this section, we perform a preliminary test on the DVCS pseudodata by using a CDNN and a QDNN to perform a local regression fit on each kinematic bin. Specifically, for a given bin, both DNNs take in the  $\phi$  values as input and the  $F$  values as output. Both DNNs have a similar architecture with 1 input layer, 10 hidden layers, and 1 output layer, and they both use the Adam optimizer with a 0.001 learning rate. In the CDNN, each input layer contains 64 perceptrons with ReLU activations. In the QDNN, each input layer contains 6 quantum perceptrons, which is equivalent to the CDNN because each quantum perceptron is a two-state quantum system. The QDNN has a classical linear preprocessing layer, angle embedding to embed classical input data into a quantum circuit, and a classical postprocessing layer with a Tanh activation function. We also use gradient clipping to prevent exploding gradients, as well as an early stop-

ping condition to prevent overfitting.

We use a normalized metric to determine the quality of the DNN regression due to the large variance in  $F$  values. Specifically, let  $F_{\text{true}}(\phi)$  be the function of connected true  $F$  values and let  $F_{\text{DNN}}(\phi)$  be the function of connected predicted  $F$  values. Then, mirroring Eq. (33), our metric  $M_{\text{reg,DVCS}}$  for the quality of the DNN fit is:

$$M_{\text{reg,DVCS}} = \frac{\int_{\phi_{\min}}^{\phi_{\max}} |F_{\text{DNN}}(\phi) - F_{\text{true}}(\phi)| d\phi}{\left| \int_{\phi_{\min}}^{\phi_{\max}} F_{\text{true}}(\phi) d\phi \right|}, \quad (51)$$

where  $\phi_{\min} = 7.5$  and  $\phi_{\max} = 352.5$ . Using the same quantum outperformance metric  $\Xi$  [Eq. (34)], we find that out of the 195 bins, the QDNN outperforms for 109 of them, and the CDNN outperforms for 86 of them.

### IX. COMPTON FORM FACTORS EXTRACTION

Extraction methods for CFFs can be broadly categorized into local fitting approaches, which determine CFFs at fixed kinematics, and deep learning-based techniques, which leverage neural networks to improve precision and accuracy. In this work, we focus exclusively on local fitting and compare two deep neural network (DNN) approaches: CDNNs and QDNNs.

Traditional local fits extract CFFs independently at each kinematic point, typically using data binned in the azimuthal angle  $\phi$ , which describes the relative orientation of the lepton and hadron scattering planes. The fitting procedure is based on the helicity amplitudes and is performed separately for each kinematic bin. While this method avoids assumptions about underlying functional forms, it can lead to non-uniqueness in extracted CFFs due to limited constraints, often resulting in large systematic uncertainties.

DNN-based fitting methods offer an alternative approach by using statistical correlations across the dataset to improve extraction precision. Unlike analytical parameterizations that impose model-specific constraints, these neural network methods learn directly from experimental data without requiring predefined functional dependencies.

We compare the performance of CDNNs and QDNNs in extracting CFFs, assessing their effectiveness through a testing phase using pseudodata generated at the same

kinematics as the experimental data. The evaluation metrics include:

Accuracy,  $\epsilon(x_B, t, Q^2)$ , which quantifies how closely the mean of the DNN-extracted CFFs aligns with the true CFF values used in pseudodata generation:

$$\epsilon(x_B, t, Q^2) = |CFF_{\text{DNN}} - CFF_{\text{true}}| \quad (52)$$

This metric is most relevant when the deviation between  $CFF_{\text{DNN}}$  and  $CFF_{\text{true}}$  remains small (i.e., less than 1). For cases with poor accuracy, precision serves as a more informative measure.

Precision,  $\sigma(x_B, t, Q^2)$ , which reflects the variation in extracted CFFs across multiple replicas:

$$\sigma(x_B, t, Q^2) = \sqrt{\frac{\sum_i (CFF_{\text{DNN}}^i - \overline{CFF_{\text{DNN}}})^2}{N}}. \quad (53)$$

The generating function used to produce the *true* CFF values follows a *basic* model, of which are described in the next section.

This study aims to compare CDNN and QDNN approaches, evaluating their ability to extract CFFs with improved accuracy and reliability. The details of the pseudodata generation, extraction methods, and corresponding results are presented in the following sections.

### A. Model Complexity

In this section, we compute values of different metrics for the complexity of the CDNN and QDNN models we use for extracting CFF values from noisy pseudodata. First, we outline the model architectures of the CDNN and QDNN. The input layer of the CDNN maps the three-dimensional input layer ( $x_B, Q^2, t$ ) to 64 neurons. Then, there are 8 hidden layers, each with 64 neurons and ReLU activation. Finally, the output layer maps the 64 features to a four-dimensional output ( $\Re\mathcal{H}, \Re\mathcal{E}, \Re\tilde{\mathcal{H}}, DVCS$ ). The input layer of the QDNN is a classical linear preprocessing layer, mapping the three-dimensional input to 6 qubits. The input data is then embedded into quantum state space using AngleEmbedding, which encodes the features as rotation angles on the qubits. Next, there are 8 hidden Strongly Entangling Layers, consisting of rotations and entanglers. Finally, the expectation value of the Pauli-Z operator for each qubit is measured. In the classical postprocessing layers, the 6 quantum outputs are mapped to 64 neurons, followed by a Tanh activation, then another linear layer to the final four-dimensional output. We now outline how to compute the number of trainable parameters and the number of floating point operations per second (FLOPs) of the CDNN and QDNN models with this prescribed architecture, and we summarize the model complexity comparison metrics in Table IV.

#### 1. Number of Trainable Parameters

For a fully connected layer with input size  $M$  and output size  $N$ , the number of trainable parameters  $P$  is

$$P = MN + N \quad (\text{weights} + \text{biases}). \quad (54)$$

For the CDNN, we have trainable parameters in the input layer ( $3 \rightarrow 64$ ), 8 hidden layers ( $64 \rightarrow 64$ ), and output layers ( $64 \rightarrow 4$ ). Therefore, the total number of trainable parameters in the CDNN is

$$\begin{aligned} P_{\text{CDNN}} &= P_{\text{in}} + 8P_{\text{hid}} + P_{\text{out}} \\ &= (3 \cdot 64 + 64) + 8(64 \cdot 64 + 64) + (64 \cdot 4 + 4) \\ &= 33796. \end{aligned} \quad (55)$$

For the QDNN, we have trainable parameters in the preprocessing layer ( $3 \rightarrow 6$ ), 8 Strongly Entangling Layers ( $6 \rightarrow 6$ ), and the postprocessing layers ( $6 \rightarrow 64 \rightarrow 4$ ). The AngleEmbedding layer is a fixed operation that contains no trainable parameters. In the Strongly Entangling Layers, each qubit undergoes three parameterized rotations, and since there are 8 Strongly Entangling Layers and 6 qubits per layer,

$$P_{\text{SEL}} = 8 \cdot 6 \cdot 3 = 144. \quad (56)$$

Therefore,

$$\begin{aligned} P_{\text{QDNN}} &= P_{\text{pre}} + P_{\text{SEL}} + P_{\text{post}} \\ &= (3 \cdot 6 + 6) + 144 + ((6 \cdot 64 + 64) + (64 \cdot 4 + 4)) \\ &= 876. \end{aligned} \quad (57)$$

#### 2. Floating Point Operations per Second (FLOPs)

FLOPs measure the computational cost of the forward pass through a DNN. For a single dense linear layer with input size  $M$  and output size  $N$ , the number of FLOPs  $C$  is

$$C = 2MN. \quad (58)$$

For the CDNN, we have the input layer ( $3 \rightarrow 64$ ), a ReLU activation (64 FLOPs), 8 hidden layers ( $64 \rightarrow 64$ ) and associated ReLU activations (64 FLOPs), and an output layer ( $64 \rightarrow 4$ ). Therefore,

$$\begin{aligned} C_{\text{CDNN}} &= (C_{\text{in}} + C_{\text{ReLU}}) + 8(C_{\text{hid}} + C_{\text{ReLU}}) + C_{\text{out}} \\ &= (2 \cdot 3 \cdot 64 + 64) + 8(2 \cdot 64 \cdot 64 + 64) + 2 \cdot 64 \cdot 4 \\ &= 67008. \end{aligned} \quad (59)$$

For the QDNN, we have the preprocessing layer ( $3 \rightarrow 6$  qubits), 8 Strongly Entangling Layers (6 qubits  $\rightarrow$

Metric	CDNN	QDNN
Depth	10 layers (2 in/out + 8 hidden)	11 layers (8 quantum + 3 classical)
Width	64 neurons	6 qubits (64-dimensional)
Trainable Parameters	33796 parameters	876 parameters
FLOPs	67008 FLOPs	74688 FLOPs

TABLE IV: DNN model complexity comparison

6 qubits), and the postprocessing layers (6 qubits  $\rightarrow$  64  $\rightarrow$  4) and a Tanh activation (64 FLOPs). Since each qubit is a two-state system and all the qubits in a layer are tensored together, the effective input and output sizes for the qubit layers is  $2^6 = 64$ . Therefore,

$$\begin{aligned}
C_{\text{QDNN}} &= C_{\text{pre}} + 8C_{\text{SEL}} + (C_{\text{post}} + C_{\text{Tanh}}) \\
&= (2 \cdot 3 \cdot 64) + 8(2 \cdot 64 \cdot 64) \\
&\quad + (2 \cdot 64 \cdot 64 + 64 + 2 \cdot 64 \cdot 4) \\
&= 74688.
\end{aligned} \tag{60}$$

## B. CFF Extraction Results

Now that we have discussed the architecture and complexity of the CDNN and QDNN models, we will outline our results documenting the quality of the CDNN and QDNN extraction of CFFs from the pseudodata sets. In Figs. 6 and 7, we display histograms of the extraction results for the three CFFs and the DVCS cross-section component from 1000 noisy replicas of the cross-section data from two selected bins. At a glance, the QDNN appears to exhibit improved accuracy and precision in the majority of cases. To determine the quality of the CDNN and QDNN fits for all of the pseudodata sets as a whole, we use a reduced  $\chi^2$  metric  $M_{\chi^2}$ , which is calculated as the sum of the reduced  $\chi^2$  values for each CFF distribution for each of the 195 bins. This means that a lower reduced  $\chi^2$  metric value for a given set indicates a better fit, and a value of 4 indicates a perfect fit. Averaging the metric values over all of the bins, we find that  $M_{\chi^2}^{\text{CDNN, avg}} \approx 78.97$  and  $M_{\chi^2}^{\text{QDNN, avg}} \approx 28.18$ . Therefore, on average, the QDNN outperforms the CDNN by around 64.3%.

The effectiveness of the QDNN CFF extraction is further demonstrated by evaluating how well the extracted CFFs reproduce the cross-section values from our pseudodata sets. Using the method described in Section IX, we compute the predicted cross-sections from the extracted CFFs and compare them to the true noisy pseudodata. In Figures 8, 9, and 10, we present results for three representative kinematic bins, plotting the mean predicted cross-section values as a function of the azimuthal angle  $\phi_x$ , along with their 68% confidence intervals. The fluctuated true cross-section points from the pseudodata sets are overlaid for reference. A key observation from these figures is that the improved precision of the QDNN extraction leads to narrower confidence inter-

vals in the predicted cross-sections across all three bins, reflecting the reduced uncertainty in the extracted CFFs.

Finally, to get a better overall picture for the performance of the DNNs, we use four different error metrics (algorithmic error, methodological error, precision, and accuracy) to compare the DNNs over all 195 bins of data points. To compute the algorithmic error, we perform the extraction on 1000 identical replicas of each bin and calculate the resulting spread of each CFF. Thus, algorithmic error represents error resulting from the limitations and inherent uncertainties of the extraction algorithm itself, rather than simulated experimental error in the data. To compute the methodological error, we introduce a spread in the parameters used to generate the CFFs (Table III) and use the generating function [Eq. (50)] to generate new noisy CFFs that approximately correspond to the spread in the original extracted CFFs. Then, the methodological error is computed as the spread of the resulting residuals from the new extractions. Thus, methodological error represents the uncertainty arising from the choice of model parameters and assumptions used in the extraction process. By introducing a spread in the parameters used to generate the CFFs and propagating this spread through the generating function, we assess how variations in these underlying assumptions influence the extracted CFF values. This approach allows us to estimate the systematic impact of modeling choices on the final extraction results, distinguishing it from purely statistical or algorithmic uncertainties. Finally, precision and accuracy are computed using Eqs. (53) and (52), respectively. These metrics provide an evaluation of the performance of the DNNs on the original pseudodata set, with precision measuring the consistency of the extracted values across multiple replicas and accuracy reflecting the agreement between the extracted and true CFFs. For all four of these error metrics, a lower value indicates a lower error.

In Figs. 11, 12, 13, and 14, we plot comparative histograms of the algorithmic error, methodological error, precision, and accuracy of the DNNs for each of the CFFs across all 195 kinematic bins. It is immediately clear that the QDNN demonstrates superior performance in methodological error, precision, and accuracy. In Fig. 14, we can see that the QDNN extraction accuracy is significantly improved for the CFFs  $\Re\mathcal{E}$  and  $\Re\tilde{\mathcal{H}}$ , but that the DNNs perform similar regarding the accuracy of  $\Re\mathcal{H}$  and DVCS extraction. For  $\Re\mathcal{H}$ , where the accuracy is generally low for both DNNs (see Fig. 6), precision is more informative metric, where the QDNN clearly outperforms (Fig. 13a). Similarly, the precision

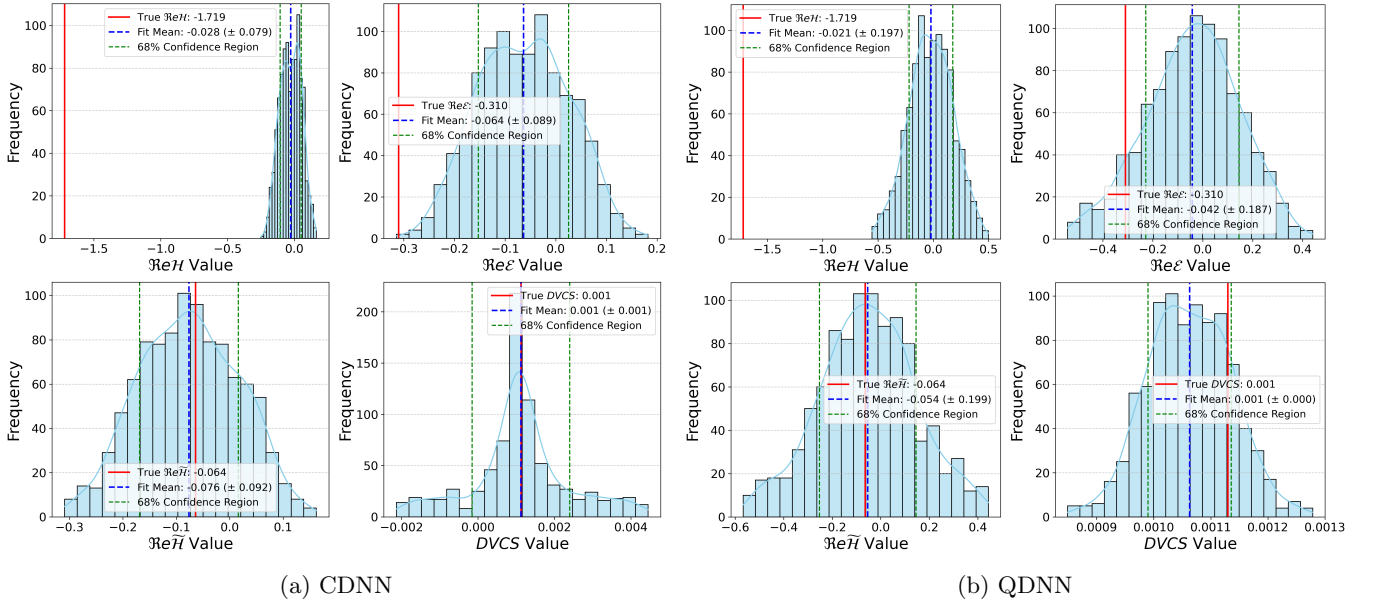


FIG. 6: Distributions of the extracted CFFs from noisy replicas of cross-section data generated from kinematics  $k = 10.992$ ,  $Q^2 = 7.12$ ,  $x_B = 0.499$ ,  $t = -0.61292$  (Set 53).

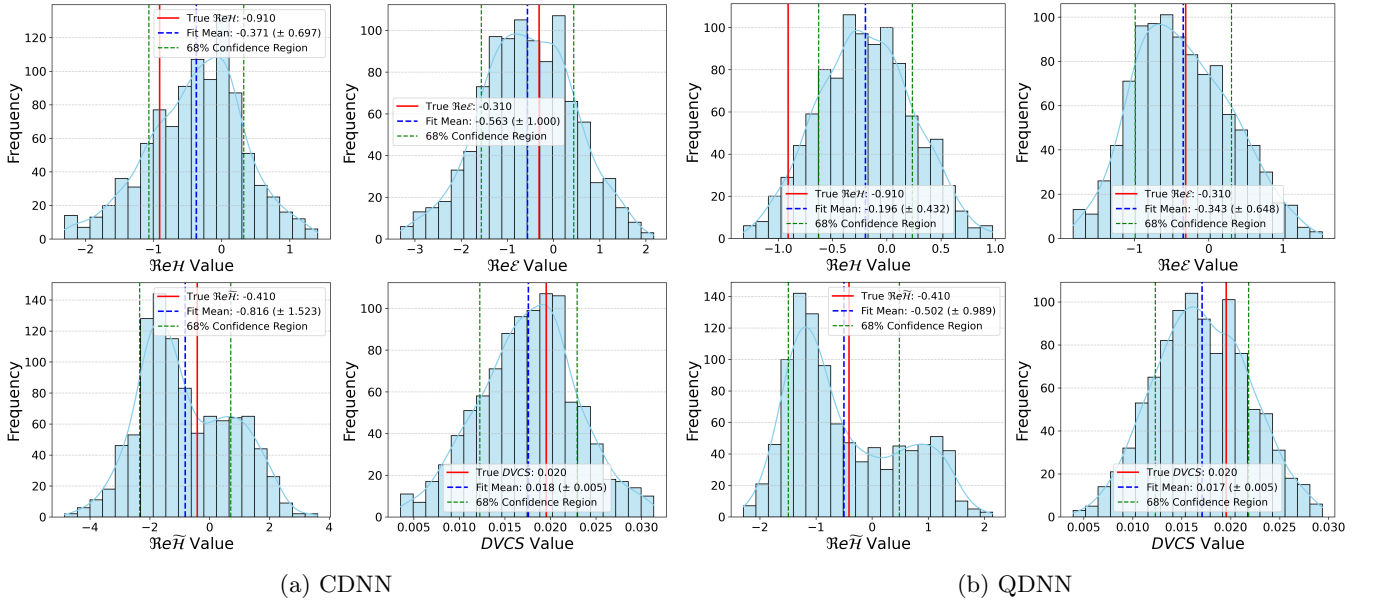


FIG. 7: Distributions of the extracted CFFs from noisy replicas of cross-section pseudodata generated from kinematics  $k = 5.75$ ,  $Q^2 = 2.22$ ,  $x_B = 0.333$ ,  $t = -0.16$  (Set 144).

of the DVCS extraction is higher for the QDNN as well (Fig. 13d). The improved precision of the QDNN in these cases ensures that despite lower accuracy for both DNNs, the extracted values remain more consistent across different replicas. Barring the aforementioned low accuracy  $\Re H$  extraction, the methodological error is consistently lower for the QDNN across all CFFs. This suggests that the QDNN is more robust to variations in the parameters used to generate the CFFs, reinforcing its advantage in

stability and resistance to systematic model uncertainties.

Despite the clear quantum outperformance with regards to the methodological error, precision, and accuracy, Fig. 11 demonstrates that the QDNN exhibits a higher algorithmic error compared to the CDNN. This result suggests that while QDNNs improve precision and accuracy in most cases, their training process introduces additional sources of uncertainty, which is a result of

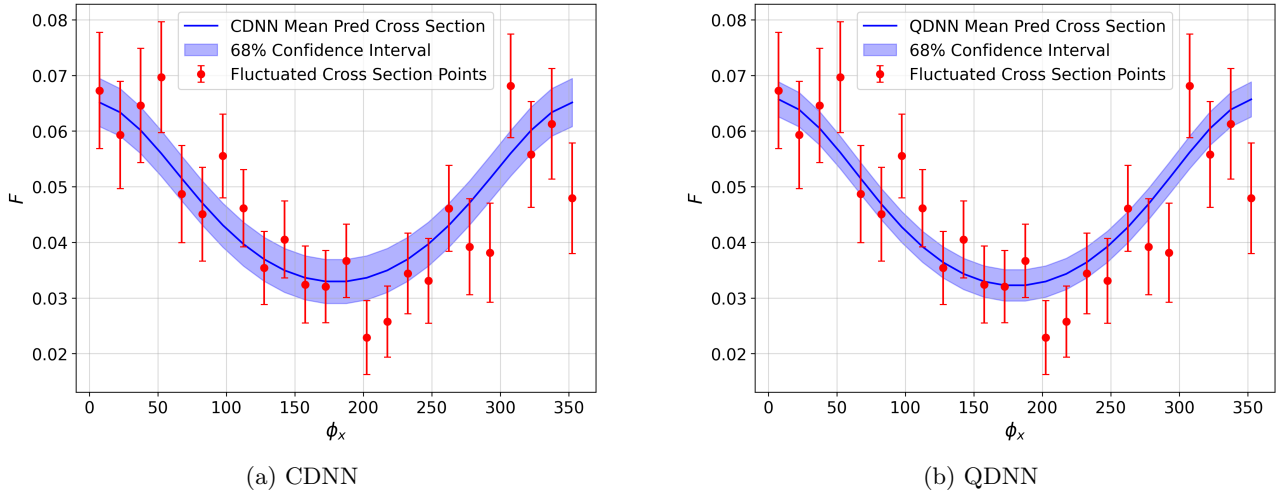


FIG. 8: Predicted cross-sections from the CDNN and QDNN fits of noisy replicas of cross-section pseudodata (red points) generated from kinematics  $k = 5.75$ ,  $Q^2 = 2.012$ ,  $x_B = 0.378$ ,  $t = -0.192$  (Set 11). The solid blue line corresponds to the mean predicted cross-sections across the different replicas, and the error bands correspond to the 68% confidence interval.

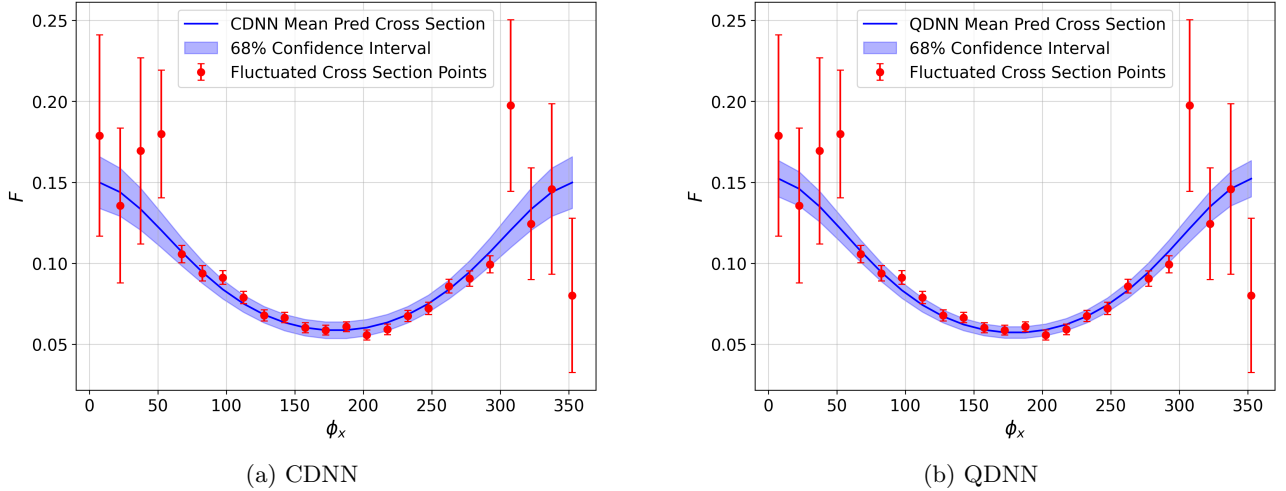


FIG. 9: Predicted cross-sections from the CDNN and QDNN fits of noisy replicas of cross-section pseudodata (red points) generated from kinematics  $k = 5.75$ ,  $Q^2 = 2.22$ ,  $x_B = 0.333$ ,  $t = -0.16$  (Set 144). The solid blue line corresponds to the mean predicted cross-sections across the different replicas, and the error bands correspond to the 68% confidence interval.

the structure of our QDNN implementation. Specifically, the increased algorithmic error in QDNNs stems from initialization and optimization challenges unique to quantum networks. Unlike classical models, QDNNs must respect constraints such as unitarity and entanglement. Our implementation uses strongly entangling layers. While this architecture is effective in capturing quantum correlations, it also makes the optimization landscape more complex. Another important challenge in training QDNNs is overcoming barren plateaus, where the gradients vanish exponentially as the number of qubits increases. To mitigate this, we use small-angle

initialization, sampling parameters from a narrow normal distribution. While this helps maintain non-vanishing gradients, it may also limit the search space and contribute to algorithmic error since it forces the QDNN to explore a constrained region of the parameter space in early training. This can slow down convergence and make the network more sensitive to local minima, leading to greater variability in the extracted CFFs across different replicas, manifesting as higher algorithmic error. Despite this higher algorithmic error, the overall extraction quality of the QDNN remains superior, suggesting that refining initialization and optimization techniques

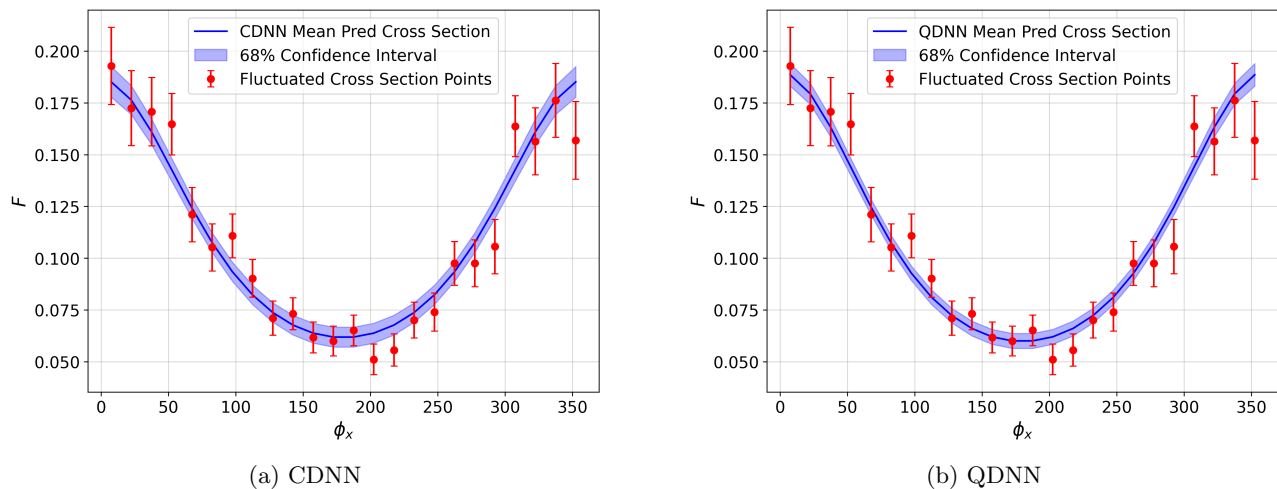


FIG. 10: Predicted cross-sections from the CDNN and QDNN fits of noisy replicas of cross-section pseudodata (red points) generated from kinematics  $k = 4.455$ ,  $Q^2 = 1.74$ ,  $x_B = 0.357$ ,  $t = -0.181$  (Set 190). The solid blue line corresponds to the mean predicted cross-sections across the different replicas, and the error bands correspond to the 68% confidence interval.

can further enhance its performance.

### C. Addressing QDNN Algorithmic Error

To systematically investigate the sources of algorithmic error in the QDNN, we implemented three new QDNN models with targeted modifications. Model 0 is our baseline QDNN, which we used for all previous CFF extraction. Even though it isn't the most optimal, it provides a simple quantum model to demonstrate the inherent quantum advantage over CDNNs in CFF extraction. Therefore, since it exhibits higher algorithmic error than our CDNN model, it is a useful starting point for identifying areas of improvement. To address these issues, we introduce Models 1-3, each focusing on a specific refinement to improve stability and reduce algorithmic error. Model 1 modifies the strongly entangling layers by adding an entanglement range parameter, limiting interactions to nearest neighbors in some cases rather than fully entangling all qubits at every layer. This aims to balance expressivity and stability, reducing excessive parameter correlations that can destabilize optimization. Model 2 focuses on addressing the barren plateau problem, where gradients vanish exponentially as the circuit depth increases. To mitigate this, Model 2 employs layerwise training, where the network begins with a shallow quantum circuit and progressively increases the number of layers over training. Additionally, it introduces depth-scaled initialization, ensuring that each layer's parameter magnitudes decrease as depth increases. This prevents excessive parameter magnitudes in deeper layers while maintaining trainable gradients throughout optimization. Model 3 refines the small-angle initialization, which is already known to help prevent barren plateaus

at initialization but may overly restrict the search space, leading to increased algorithmic error. Instead of reducing the initial weight magnitudes across layers, Model 3 rescales small-angle initialization to maintain better trainability without completely restricting parameter exploration.

To test these new models, we perform the CFF extraction on 1000 identical noisy replicas of Set 144 (see Figs. 7 and 9) using each of these four models and display the algorithmic error results in Table V. Comparing the results of Model 0 with Figure 11, we observe that the algorithmic errors for this kinematic bin align relatively well with the average algorithmic errors of the extracted CFFs across all bins. Performing the extraction with the improved QDNN models, the algorithmic error improves significantly for all three models. Table V indicates that Model 1 produces the lowest algorithmic errors for  $\Re\mathcal{H}$ ,  $\Re\mathcal{E}$ , and  $\Re\tilde{\mathcal{H}}$ , while Model 2 produces the lowest algorithmic error for  $DVCS$ . Although these new models aim to improve QDNN algorithmic error, we also examine their effect on the other three error metrics (methodological error, precision, and accuracy) and display the results in Table V. As expected, the improved algorithmic error results in better precision across Models 1-3, with the improved precision following a similar pattern to the algorithmic error. We find that these new models do not significantly affect the methodological error or accuracy.

The QDNN algorithmic error improvements observed from Models 1-3 are more comparable to the algorithmic errors from the CDNN extraction (see Fig. 11) and suggest key strategies for reducing algorithmic error and improving precision in quantum deep learning models for CFF extraction. Specifically, by refining entanglement structure, implementing layerwise training, and adjust-

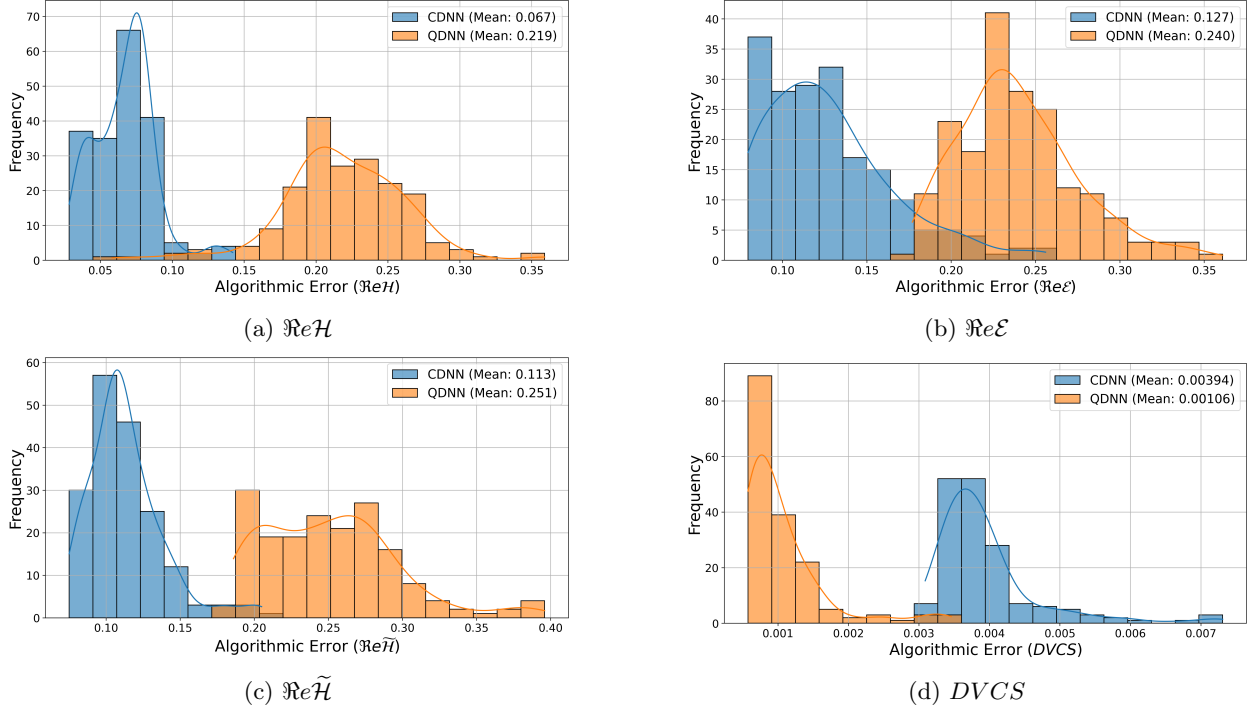


FIG. 11: Comparative histograms of the algorithmic error for the CDNN (blue) and QDNN (orange) extraction across all kinematic bins. Algorithmic error isolates uncertainty in the extraction process itself. The QDNN shows higher algorithmic error due to quantum-specific challenges such as constrained initialization and complex optimization landscapes.

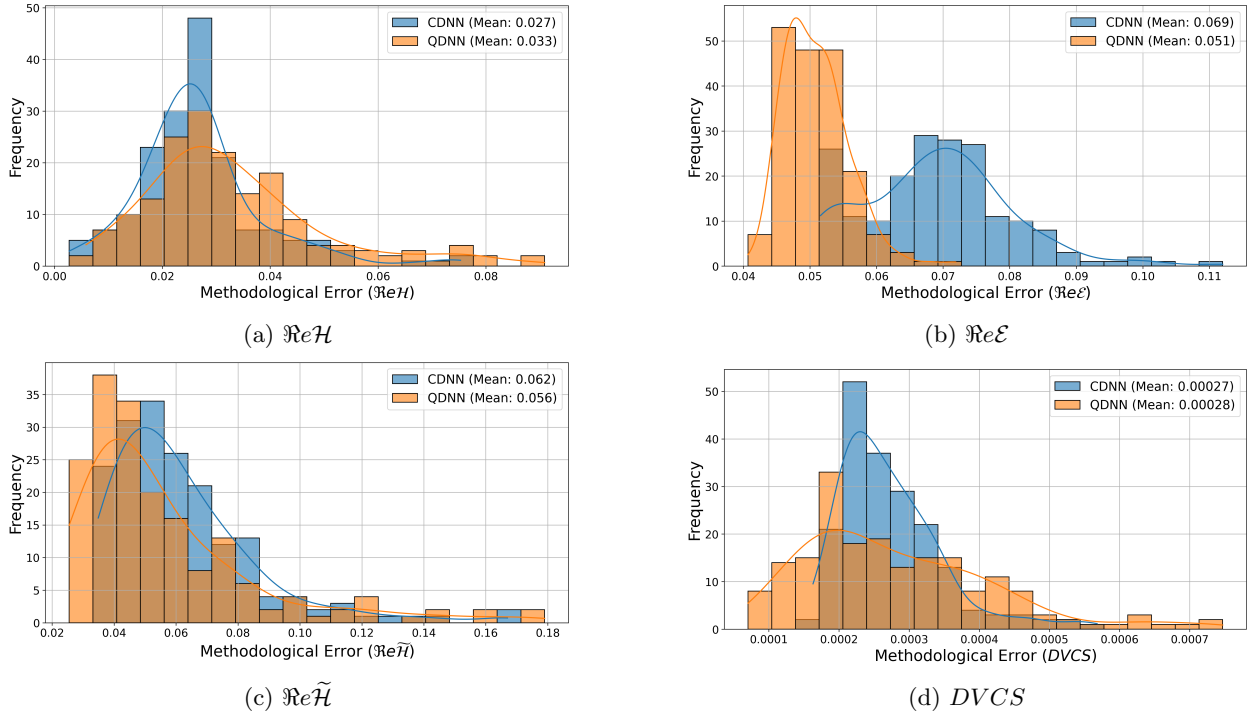


FIG. 12: Comparative histograms of the methodological error for the CDNN (blue) and QDNN (orange) extraction across all kinematic bins. Methodological error captures uncertainty arising from model assumptions and parameter choices. The QDNN consistently demonstrates lower methodological error, highlighting its robustness to systematic uncertainties.

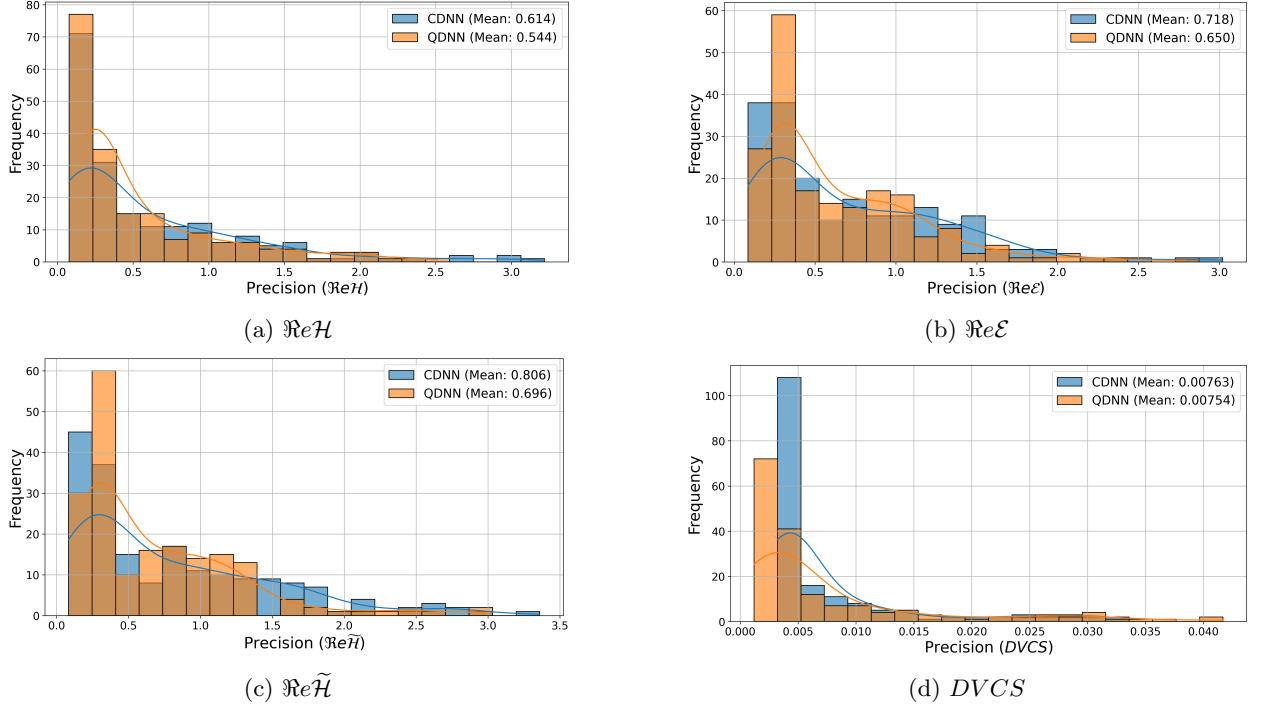


FIG. 13: Comparative histograms of the the CDNN (blue) and QDNN (orange) extraction precision across all kinematic bins. Precision reflects consistency across runs, regardless of proximity to the true value. The QDNN achieves higher precision for all CFFs, ensuring more stable and reliable extractions even in regions where accuracy is lower.

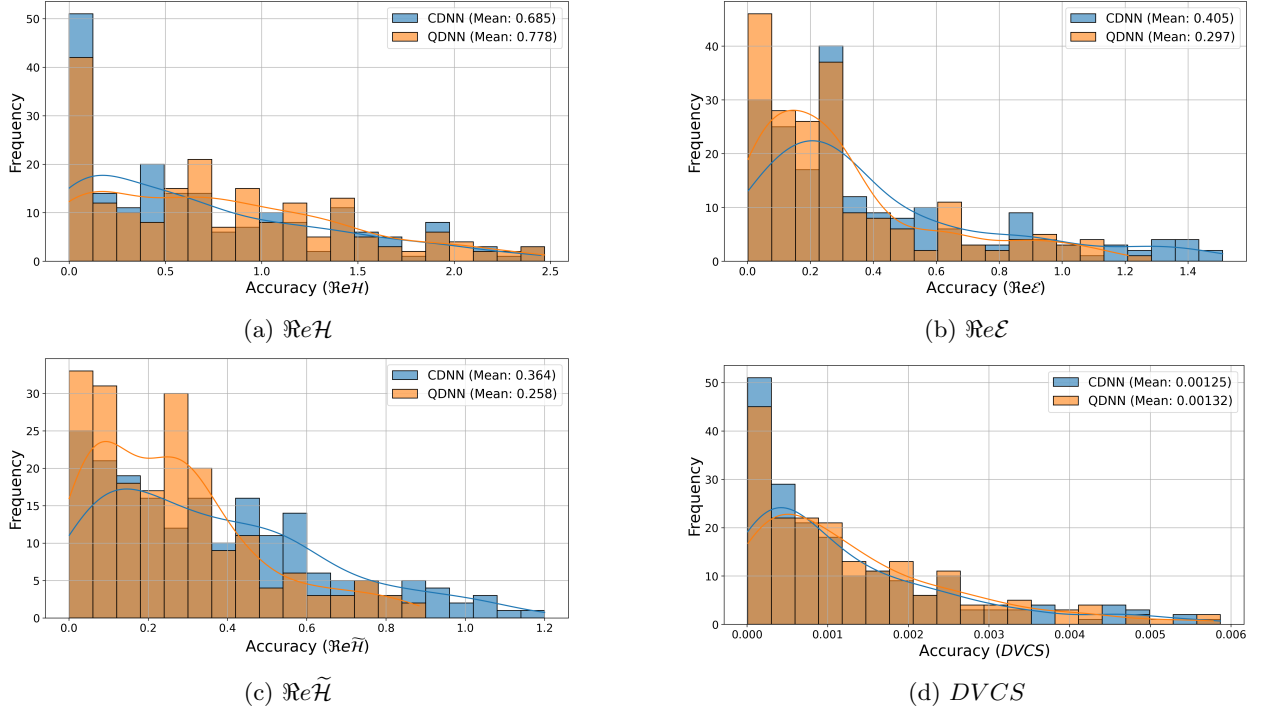


FIG. 14: Comparative histograms of the CDNN (blue) and QDNN (orange) extraction accuracy across all kinematic bins. Accuracy measures how close the DNN extractions are to the true CFFs. The QDNN shows markedly improved accuracy for  $\Re\mathcal{E}$  and  $\Re\tilde{\mathcal{H}}$ .



Model	Algorithmic Error				Methodological Error				Precision				Accuracy			
	$\Re\mathcal{H}$	$\Re\mathcal{E}$	$\Re\tilde{\mathcal{H}}$	$DVCS$	$\Re\mathcal{H}$	$\Re\mathcal{E}$	$\Re\tilde{\mathcal{H}}$	$DVCS$	$\Re\mathcal{H}$	$\Re\mathcal{E}$	$\Re\tilde{\mathcal{H}}$	$DVCS$	$\Re\mathcal{H}$	$\Re\mathcal{E}$	$\Re\tilde{\mathcal{H}}$	$DVCS$
0	0.174	0.241	0.241	0.00227	0.0395	0.0482	0.0412	0.000208	0.454	0.652	1.02	0.00520	0.759	0.0110	0.0495	0.00259
1	0.135	0.169	0.170	0.00258	0.0405	0.0468	0.0367	0.000339	0.372	0.529	0.851	0.00638	0.765	0.0632	0.0351	0.00252
2	0.147	0.191	0.196	0.000559	0.0395	0.0471	0.0360	0.000153	0.416	0.573	0.870	0.00498	0.752	0.0389	0.0264	0.00255
3	0.137	0.177	0.173	0.00241	0.0404	0.0469	0.0373	0.000260	0.376	0.531	0.852	0.00533	0.764	0.0604	0.0321	0.00260

TABLE V: The breakdown of the QDNN error contributions are listed for model 0-3, as described in the text, for each CFF and DVCS term.

ing initialization schemes, we demonstrate that targeted modifications can significantly enhance training stability and overall model reliability. These tests provide a foundation for future studies to develop more optimized QDNN architectures, particularly by exploring adaptive entanglement strategies, hybrid classical-quantum initialization techniques, and quantum-specific optimizers.

## X. CONCLUSIONS

In this work, we explored the application of QDNNs for the extraction of CFFs from Deeply Virtual Compton Scattering (DVCS) pseudodata and performed a systematic comparison with CDNNs under matched model complexity. To enable a direct head-to-head comparison of algorithmic performance, we deliberately constrained the QDNN architecture, ensuring parity in complexity and hyperparameter tuning between the quantum and classical models. This allowed us to isolate the effect of quantum computational mechanisms—such as entanglement and superposition—from differences in network capacity or training depth.

We developed a novel set of quantum qualifiers to identify the specific regimes—characterized by data dimensionality, function complexity, and training sparsity—where QDNNs offer the greatest advantage. These metrics extend beyond traditional performance evaluation by predicting scenarios where QDNNs are expected to outperform based on intrinsic data complexity. Through both classification and regression tasks, these quantum metrics consistently revealed enhanced performance of QDNNs in learning nontrivial correlations and high-dimensional feature spaces more efficiently than their classical counterparts.

Our application of QDNNs to DVCS pseudodata demonstrated significantly improved extraction of CFFs, with QDNNs achieving higher accuracy, greater precision, and lower total methodological error compared to CDNNs. Notably, while total error was reduced, QDNNs exhibited larger algorithmic error in some cases, likely arising from quantum-specific challenges such as restricted initialization schemes, gradient propagation lim-

itations, and entanglement-induced parameter correlations. These findings highlight areas for targeted optimization in future QDNN architectures.

To maintain parity for comparison, the QDNNs in this work were not fully optimized—nor was a QDNN-specific extraction scheme developed. As such, the true potential of quantum-enhanced inference remains only partially tapped. Future work should focus on building tailored QDNN extraction frameworks, exploring alternative initialization methods such as amplitude embedding, incorporating quantum-specific optimizers (e.g., quantum natural gradient descent), and systematically investigating how entanglement influences learning dynamics and generalization.

Ultimately, this study provides a first step toward quantum-enhanced parameter extraction in hadronic physics. The demonstrated advantage of QDNNs in capturing high-dimensional quantum correlations positions them as a promising tool for future analyses—not only in DVCS but across a range of deep exclusive processes. As quantum hardware continues to mature, and as hybrid quantum-classical learning algorithms improve in stability and scalability, QDNNs may become essential in realizing high-precision, model-independent extractions of hadronic observables. Future work will extend these methods to real experimental data, further developing quantum deep learning as a transformative approach for unraveling the structure of matter at the most fundamental level.

## XI. ACKNOWLEDGMENT

The Deep Neural Network models used in this work were trained using the University of Virginia’s high-performance computing cluster, Rivanna. The authors acknowledge Research Computing at the University of Virginia for providing computational resources and technical support that have contributed to the results reported in this publication. URL: <https://rc.virginia.edu>. This work was supported by the DOE contract DE-FG02-96ER40950.

	(26)	(27)	(28)	(29)	(30)	(31)
$\mathfrak{N}$	0.982	0.995	0.996	0.939	0.775	0.983
$\Phi$	26	29	36	27	25	28
$\mathfrak{D}$	1.637	1.491	1.679	1.488	1.525	1.531
$\mathfrak{M}$	0.648	0.762	0.504	0.833	0.784	0.622
$\mathfrak{F}$	5218.538	12459.751	13568.363	14724.023	18429.203	6100.399

TABLE VI: Function characteristic data [nonlinearity ( $\mathfrak{N}$ ), frequency complexity ( $\Phi$ ), fractal dimension ( $\mathfrak{D}$ ), mutual information ( $\mathfrak{M}$ ), and Fourier transform complexity ( $\mathfrak{F}$ )] for regression target functions [Eqs. (26)-(31)] with  $0.1\sigma$  noise level.

	(26)	(27)	(28)	(29)	(30)	(31)
$\mathfrak{N}$	0.986	0.994	0.994	0.942	0.778	0.983
$\Phi$	31	31	36	28	25	30
$\mathfrak{D}$	1.618	1.533	1.684	1.518	1.547	1.553
$\mathfrak{M}$	0.667	0.607	0.453	0.752	0.791	0.625
$\mathfrak{F}$	5821.253	12971.771	13408.041	14705.103	17651.770	6016.843

TABLE VII: Function characteristic data for regression target functions [Eqs. (26)-(31)] with  $0.25\sigma$  noise level.

	(26)	(27)	(28)	(29)	(30)	(31)
$\mathfrak{N}$	0.997	0.997	1.000	0.963	0.879	0.977
$\Phi$	33	35	36	29	33	26
$\mathfrak{D}$	1.609	1.638	1.715	1.517	1.586	1.665
$\mathfrak{M}$	0.468	0.458	0.497	0.541	0.585	0.485
$\mathfrak{F}$	14419.142	22150.011	27217.273	24568.751	32359.330	15787.680

TABLE VIII: Function characteristic data for regression target functions [Eqs. (26)-(31)] with  $1\sigma$  noise level.

Epochs	(26)	(27)	(28)	(29)	(30)	(31)
10	3.818	5.373	5.929	6.164	6.921	3.857
50	2.348	4.272	5.818	4.592	4.688	3.166
100	1.700	3.670	5.524	3.183	3.841	2.980
250	0.249	1.790	4.784	2.286	3.277	1.366
500	0.382	1.162	4.345	1.879	3.295	0.922

TABLE IX: Regression metric  $M_{\text{reg}}$  values for CDNN regression on 100 data points generated from the target functions [Eqs. (26)-(31)] with  $0.1\sigma$  noise level.

Epochs	(26)	(27)	(28)	(29)	(30)	(31)
10	3.151	4.603	5.877	4.490	4.350	3.416
50	0.183	2.859	5.790	3.310	3.929	2.183
100	0.191	2.335	5.682	1.833	3.604	1.616
250	0.204	2.165	5.576	1.291	3.341	1.589
500	0.209	0.975	5.462	1.171	3.289	0.433

TABLE X: Regression metric  $M_{\text{reg}}$  values for QDNN regression on 100 data points generated from the target functions [Eqs. (26)-(31)] with  $0.1\sigma$  noise level.

Epochs	(26)	(27)	(28)	(29)	(30)	(31)
10	3.824	5.373	5.928	6.164	6.921	3.859
50	2.259	4.242	5.772	4.624	4.705	3.137
100	1.937	3.689	5.531	3.065	3.868	3.007
250	0.554	2.754	5.029	2.244	3.410	1.666
500	0.622	1.572	4.686	2.077	3.441	1.188

TABLE XI: Regression metric  $M_{\text{reg}}$  values for the CDNN regression on 100 data points generated from the target functions [Eqs. (26)-(31)] with  $0.25\sigma$  noise level.

Epochs	(26)	(27)	(28)	(29)	(30)	(31)
10	3.697	4.620	5.964	4.503	4.301	3.438
50	0.388	2.978	5.748	3.337	4.064	3.030
100	0.444	2.382	5.698	2.030	3.800	1.833
250	0.445	1.642	5.613	1.658	3.518	1.081
500	0.581	1.400	5.493	1.455	3.582	0.946

TABLE XII: Regression metric  $M_{\text{reg}}$  values for the QDNN regression on 100 data points generated from the target functions [Eqs. (26)-(31)] with  $0.25\sigma$  noise level.

Epochs	(26)	(27)	(28)	(29)	(30)	(31)
10	3.865	5.371	5.923	6.164	6.922	3.881
50	3.431	4.228	5.711	4.940	4.905	3.663
100	2.593	3.500	5.602	3.707	4.515	3.459
250	2.633	3.842	5.855	3.596	4.633	2.985
500	2.215	3.390	5.528	3.015	4.429	2.904

TABLE XIII: Regression metric  $M_{\text{reg}}$  values for the CDNN regression on 100 data points generated from the target functions [Eqs. (26)-(31)] with  $1\sigma$  noise level.

Epochs	(26)	(27)	(28)	(29)	(30)	(31)
10	3.697	4.815	5.913	4.785	5.008	3.633
50	1.453	3.352	5.905	3.906	4.611	3.508
100	1.661	3.069	5.781	3.430	4.480	3.270
250	2.030	2.907	5.778	3.007	4.449	2.464
500	2.635	3.341	4.832	3.222	4.471	3.052

TABLE XIV: Regression metric  $M_{\text{reg}}$  values for the QDNN regression on 100 data points generated from the target functions [Eqs. (26)-(31)] with  $1\sigma$  noise level.

Epochs	0.75 to 1 $\mathfrak{N}$	25 to 35 $\Phi$	1.45 to 1.75 $\mathfrak{D}$	0.45 to 0.85 $\mathfrak{M}$	5000 to 35000 $\mathfrak{F}$
10	-2.43	-0.0386	-1.69	1.12	7.06E-06
50	0.209	-0.0257	-1.89	0.725	-8.55E-06
100	1.36	-0.0327	-2.66	0.87	-3.04E-05
250	0.715	-0.0115	-1.26	0.379	-5.59E-06
500	0.746	-0.0476	-1.64	1.1	-2.26E-05
Average	0.12	-0.0312	-1.83	0.839	-1.20E-05
Average $\Delta\Xi$ over domain	0.03	-0.312	-0.549	0.337	-0.36

TABLE XV: Slopes of linear regressions on the quantum outperformance  $\Xi$  against the function characteristics [nonlinearity ( $\mathfrak{N}$ ), frequency complexity ( $\Phi$ ), fractal dimension ( $\mathfrak{D}$ ), mutual information ( $\mathfrak{M}$ ), and Fourier transform complexity ( $\mathfrak{F}$ )] for DNN target function regression. The approximate range in the function characteristics, the average slopes across the different epochs, and the average change in  $\Xi$  over the function characteristic domain are reported.

Epochs	$\mathfrak{N}$	$\Phi$	$\mathfrak{D}$	$\mathfrak{M}$	$\mathfrak{F}$
10	0.829	0.573	0.384	0.524	0.079
50	0.008	0.306	0.596	0.267	0.12
100	0.104	0.155	0.368	0.13	0.467
250	0.032	0.023	0.096	0.027	0.022
500	0.022	0.246	0.102	0.144	0.228
Average	0.199	0.261	0.309	0.218	0.183

TABLE XVI:  $R^2$  values of linear regressions on the quantum outperformance  $\Xi$  against the function characteristics [nonlinearity ( $\mathfrak{N}$ ), frequency complexity ( $\Phi$ ), fractal dimension ( $\mathfrak{D}$ ), mutual information ( $\mathfrak{M}$ ), and Fourier transform complexity ( $\mathfrak{F}$ )] for DNN target function regression. The average  $R^2$  values across the different epochs are reported.

- 
- [1] A V Belitsky, D Müller, and A Kirchner. *Nucl. Phys. B*, 629:323, 2002.
- [2] A. V. Belitsky and D. Müller. *Phys. Rev. D*, 79:014017, 1 2009.
- [3] A. V. Belitsky and D. Müller. *Phys. Rev. D*, 82:074010, 10 2010.
- [4] A. V. Belitsky, D. Müller, and Y. Ji. *Nucl. Phys. B*, 878:214–268, 1 2014.
- [5] V. M. Braun, A. N. Manashov, D. Müller, and B. M. Pirnay. *Phys. Rev. D*, 89:074022, 4 2014.
- [6] Yuxun Guo, Xiangdong Ji, Brandon Kriesten, and Kyle Shiells. *JHEP*, 06:096 (2022), 6 2022.
- [7] Krešimir Kumeriški, Dieter Müller, and Andreas Schäferd. *JHEP*, 07:073 (2011), 2011.
- [8] H. Moutarde, P. Sznajder, and J. Wagner. *Eur. Phys. J. C*, 79:614, 7 2019.
- [9] B. D. Ripley. New York, NY, USA.
- [10] Alessandro Bacchetta, Umberto D’Alesio, Markus Diehl, and C. Andy Miller. *Phys. Rev. D*, 70:117504, 12 2004.
- [11] J. J. Kelly. Simple parametrization of nucleon form factors. *Phys. Rev. C*, 70:068202, 12 2004.
- [12] Xiangdong Ji. *Phys. Rev. D*, 55:7114, 6 1997.
- [13] X. Ji and J. Osborne. One-loop corrections and all order factorization in deeply virtual Compton scattering. *Physics Review D*, 58:094018, 1997.
- [14] B. E. White. Factorisation in deeply virtual Compton scattering: Local ope formalism and structure functions. *Journal of Physics G*, 28:203, 2001.
- [15] M Diehl. Generalized parton distributions. *Phys. Rep.*, 388:41–277, 2003.
- [16] V. Bertone, H. Dutrieux, C. Mezrag, H. Moutarde, and P. Sznajder. Deconvolution problem of deeply virtual Compton scattering. *Phys. Rev. D*, 103(11):114019, 2021.
- [17] F. Georges and et al. (Jefferson Lab Hall A Collaboration). *Phys. Rev. Lett.*, 128:252002, 6 2022.
- [18] Y. Du, M.-H. Hsieh, T. Liu, and D. Tao. Expressive power of parametrized quantum circuits. *Physical Review Research*, 2(3):033125, 2020.
- [19] F. Shen and J. Liu. Qfcnn: Quantum fourier convolutional neural network. *arXiv preprint arXiv:2106.10421*, 2021.
- [20] G. Verdon, J. Pye, and M. Broughton. Interpretable quantum advantage in neural sequence learning. *PRX Quantum*, 4(2):020338, 2023.
- [21] Y. Chen, Z. Zhu, C. Zhai, M. Ying, and Y. Shi. Quantum neural networks in practice: A comparative study with classical counterparts. *arXiv preprint arXiv:2411.19276*, 2024.
- [22] S. J. Wetzel and M. Scherzer. Quantum convolutional neural networks for high energy physics data analysis. *Physical Review Research*, 4(1):013231, 2022.
- [23] J. J. Kim, D. Kim, and S. H. Kim. A new index of nonlinearity for nonlinear time series analysis. *Physica A: Statistical Mechanics and its Applications*, 391(4):1293–1300, 2012.
- [24] T. W. Sederberg, M. D. Holmes, and A. K. Cohen. Fourier complexity and its application to eeg signal classification. *Biomedical Signal Processing and Control*, 14:125–131, 2014.
- [25] P. G. M. van Mierlo and M. W. J. Smeulders. A box-counting algorithm for estimating the fractal dimension of grayscale images. *Physica A: Statistical Mechanics and its Applications*, 252(1-2):267–278, 1998.
- [26] A. Kraskov, H. Stögbauer, and P. Grassberger. Estimating mutual information. *Physical Review E*, 69(6):066138, 2004.
- [27] P. Stoica and R. Moses. *Spectral Analysis of Signals*. Pearson Prentice Hall, 2005.
- [28] M. Defurne and et al. (Jefferson Lab Hall A Collaboration). *Nat. Commun.*, 8:1408, 12 2017.
- [29] M. Defurne and et al. (Jefferson Lab Hall A Collaboration). *Phys. Rev. C*, 92:055202, 11 2015.
- [30] H. S. Jo and et al. (CLAS Collaboration). *Phys. Rev. Lett.*, 115:212003, 11 2015.